POLITECNICO DI MILANO

Facoltá di Ingegneria Industriale

Corso di Laurea in Ingegneria Aerospaziale

PRELIMINARY EVALUATION OF REAL GAS EFFECTS IN A GASDYNAMIC NOZZLE

Relatore: Prof. A. Guardone

Correlatori: Prof. P. Colonna
Prof. R. Pecnik
Ing. D. Pasquale

Davide Brambilla 734013

Anno Accademico 2009/2010

Abstract

The harmful influence of large-scale fossil utilization on the climate enhanced the need to exploit renewable heat sources such as solar radiation or geothermal heat. In this view, the Organic Rankine Cycle is an attractive option for small- and medium-scale applications (from approximately 100 kW_e up to 2 MW_e). However, the characteristics of the organic fluids and the conditions in which this apparatus operates, require complex thermodynamic modeling and often involves highly supersonic flows. Therefore, the design of turboexpanders is very difficult because conventional methods based on similarity criteria do not apply and the experience in the field of organic compounds is very limited.

Therefore the present work proposes a methodology can be ultimately applied to the design of turbine blades. Such an approach couples fluid-dynamic analysis with a Genetic Algorithm for the optimization. In particular, the thesis' aim is to optimize the shape of a two dimensional converging-diverging nozzle for an organic compound to achieve given outflow conditions. Moreover, different levels of approximation are evaluated: ideal- and real-gas laws for the thermodynamics, while inviscid and viscous flows for the fluid-dynamics. In the end, such problem resembles a turbine expansion and has an immediate application to a wind tunnel for organic fluids currently under construction at the Politecnico di Milano.

Keywords: nozzle, real-gas, optimization, inviscid, viscous

Sommario

L'influenza nociva all'ambiente dell'impiego di combustibili fossili su larga scala ha aumentato il bisogno di sfruttare risorse di energia rinnovabili come la radiazione solare o il calore geotermico. In questa ottica, il Ciclo Rankine Organico é un'opzione attraente per applicazioni di piccola e media scala (da circa 100 kW_e fino a 2 MW_e). Tuttavia, le condizioni di impiego dei fluidi organici sono caratterizzate una termodinamica complessa che spesso coinvolge anche flussi altamente supersonici. Perció, il progetto di turbine é molto difficoltoso poiché i metodi convenzionali basati sui criteri di similitudine non possono essere applicati e l'esperienza nel settore per ora molto limitata.

Quindi il presente lavoro propone una metodologia che potrá essere utilizzata per il progetto di palette di turbine. Tale approccio accoppia calcoli fluidodinamici con un Algoritmo Genetico per l'ottimizzazione. In particolare, la tesi si occupa di ottimizzare la forma di un ugello convergente-divergente bidimensionale per un fluido organico al fine di ottenere le condizioni di scarico desiderate. Inoltre, si valutano diversi livelli di approssimazione: per la termodinamica si considera sia la legge di stato del gas ideale, sia una rappresentazione piú accurata come gas reale, mentre per le analisi fluidodinamiche sono analizzati sia flussi inviscidi che viscosi. Infine, il problema assomiglia un'espansione in turbina ed ha un immediata applicazione in una galleria del vento per fluidi organici al Politecnico di Milano.

Parole chiave: ugello, gas-reale, ottimizzazione, inviscida, viscosa

Contents

List of Figures

List of Tables

Chapter 1

Introduction

– So what's the plan, I know you got one, so you might as well tell me what it is?

1.1 Background

The strong economic growth that many developed countries have experienced during the last two centuries was made possible by the large-scale utilization of fossil energy sources such as coal, oil and natural gases. The current depletion of easily accessible fossil energy reserves combined with the exponentially growing world energy consumption has led to fossil-based energy becoming a scarce commodity, as indicated by its continuous upward price trends. Moreover, the harmful influence of larce-scale fossil utilization on environment and climate, enhance the need of being able to exploit renewable energy sources such as solar radiation or geothermal heat [1]. In this view, the organic Rankine Cycle (ORC) technology seems to be an attractive option.

The main difference between ORCs and conventional Rankine Cycles using steam is the use of an organic compound as working fluid, which allows for the optimal design of the cycle depending on both the power output desired and the source/sink temperatures [2]. In fact, for small- to medium-scale applications (from approximately 100 kW_e up to 2 MW_e), organic fluids allow to achieve high isentropic efficiency in the turbine, which would not be possible if steam were the process medium.

The working fluid is found to enter the turbine stages in the so-called dense gas region, namely it is in a thermodynamic state close to the critical point in which the ideal gas approximation no longer holds. In this view, the fluid-dynamic behavior of the ORC turbine may differ significantly from the predicted one if the design process neglects the real gas effects. Therefore, one of the challenges to fully exploit the ORC technology is the optimal fluid-dynamic design of turbomachinery operating at these particular thermodynamic conditions.

1.2 Motivations

This thesis deals with the fluid-dinamic design of turbomachinery for ORC applications. To understand the impact of the turbine on the cycle performance, here is an example. Consider a regenerative Organic Rankine Cycle with D_4 as the working fluid for low power outputs and receiving power from biomass combustion. Firstly, suppose the following heat source parameters:

- mass flow $\dot{m}_{\mathrm{HS}} = 4.5\ kg/s$;
- inflow temperature $T_{\mathrm{HS}} = 350^{o}C$.

Then, the cycle maximum temperature cannot exceed $T_{max} = 305^{o}C$ because of the thermal stability limit of the working fluid, while the minimum temperature is fixed at $T_{min} = 103.5^{o}C$ by the cold sink. The top and bottom pressures are respectively $P_{max} = 10\ bar$ and $P_{min} = 0.1\ bar$ (figure 1.1). Now, table 1.1 examines the impact of a one-percentage point increase in the tubine efficiency on the energy output over one year (8000 hours). Supposing an energy cost of 0.07 Euro/kWh [3], it allows a save of 595 Euro every year for every unit. By projecting such savings over many years and many units, these figures become very interesting, and justify an investment for even a slight improvement of the turbomachinery performance.

1.3 Objectives

The aim of the present work is the design of a two dimensional nozzle working with an organic fluid to achieve the desired outflow. On the one hand, the expansion occurring in such a geometry resembles the one in a turbine stator

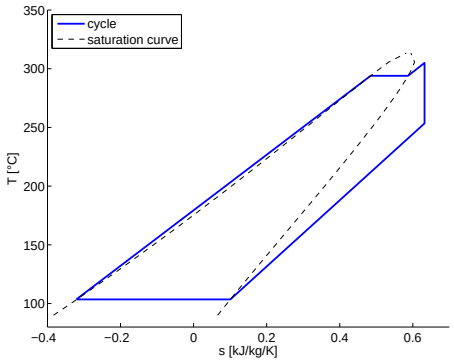

Figure 1.1: Organic Rankine Cycle considered in the example, representation in the $T - s$ plane

Table 1.1: Impact on the cycle of a 1% increase in the turbine efficiency

turbine efficiency	80%	81%
mass flow $[kg/s]$	2.381	2.377
electric power output $[kW_e]$	106.30	107.35
energy over 1 year $[MWh]$	850.4	858.9

while, on the other hand, it has a direct application in the TROVA[1] wind tunnel under construction at Politecnico di Milano for the calibration of turbine probes. The exemplary conditions analyzed aim to show where the non-ideal behavior of the gas becomes relevant.

The standard procedure to design a supersonic nozzle of minimal length with uniform outflow is based on the Method of Characteristics (MoC), which is thoroughly explained by Zuchrov and Hoffman [4]. However, that methodology allows only to design the diverging part of the duct, since the characteristic lines do not exist in the subsonic flowfields, therefore the converging part is left undefined. Furthermore, the Method of Characteristics deals with inviscid flows only, being unable to evaluate the viscous effects, or turbulence.

The present work employs a Genetic Algorithm together with a Computationa Fluid Dynamic (CFD) solver to optimize the shape of the nozzle for the desired outflow, extending the work by Pasquale [5] to the real gas

[1]Test Rig for Organic Vapors

Table 1.2: Projection on the save of money (thousands of Euros) with a 1% increase in the turbine efficiency

units	1	50	1000
years			
1	0.60	29.75	595.00
5	2.98	148.75	2975.00
10	5.95	297.50	5950.00
15	8.93	446.25	8925.00

models and viscous flows. In fact, the limits of this approach are mainly due to the abilities of the CFD program to handle the different aspects, so that the viscous effects can be accounted for in the design, if the flow solver can. Moreover, the approach allows to evaluate what happens to the outflow uniformity if the nozzle has a shorter length than the MoC design. For instance, this feature allows for compromises if the standard MoC design would be not feasable in practice.

Finally, the coupling of a Genetic Algorithm with a CFD solver is very expensive in terms of computational resources, but nowadays the methodology has become affordable. Future plans aim at extending it to the design of complex turbomachinery for ORC applications, where it seems the only viable way. In fact, the interaction between subsonic and supersonic flows together with the complex geometries of a turbine stage make the MoC almost useless.

1.4 Contents

The following three chapters offer an overview on the fundamental aspects of the work, while the results are presented afterwards.

In particular, **chapter 2** resumes the main features of the ORC technology. Besides reporting the cycle configuration, the focus is placed on the use of an organic fluid in place of steam, the flexibility it offers to the designer and the advantage for a certain range of power outputs. Finally, a brief description of the TROVA facility is given, which represents the most direct application of this work.

Then, since in the ORCs the organic compounds tend to operate in thermodynamic states close to the critical point, the behavior of the fluid might differ from the predicted one if the so-called "real gas effects" are not accounted for. **Chapter 3** explains what such effects are and underlines the importance of using accurate thermodynamic models.

Successively, **chapter 4** defines a general optimization problem: the design variables, the objectives and the constraints. The possible methods to reach the optimal solution are discussed, but only the Genetic Algorithms are selected. They mimic the process of natural selection beginning from an initial set of candidate designs: at the end of the evolution only the fittest individuals survive. In case of fluid dynamic optimization, the Genetic Algorithm interacts with a flow solver to evaluate the quality of each individual: understandably, this direct approach might be very expensive in terms of computational resources. Therefore, sometimes surrogate models can be used in place of the flow solver to improve the time efficiency of the method without losing its effectiveness. This approach is useful in many engineering branches and can be succesfully applied to the design of turbomachinery components, especially when unconventional gasdynamics comes into play.

The applicative part of the thesis starts with **chapter 5**. Here, a two dimesional converging-diverging nozzle is selected to inverstigate the real gas effects, because it is the simplest geometry able to reproduce the same expansion occurring in an ORC turbine. Since the Genetic Algorithm handles a limited set of variables, the goal of this chapter is to describe the selected geometry with the least set of parameters.

The following **chapter 6** tests the methodology by performing the optimization according to a politropic ideal-gas and inviscid-flow models. The selected fluid is MDM, a siloxane, here assumed to be in the ideal gas region. The notions of design variables and objective functions are applied to the specific problem. Even though the simplicity of both the geometry and the flow model might make this aspect superfluous, surrogate models are thoroughly evaluated, because of their foreseen importance in the design of complex turbomachinery components.

Then, **chapter 7** improves the previous optimization employing an accurate real-gas thermodynamic model. The analyzed expansion starts from supercritical conditions, passes very close to the saturation curve and ends in a highly supersonic condition. The non-ideality of the fluid emerges also from a one-dimensional analysis, leading to a huge difference in the area ratios with

respect to the ideal gas prediction. Actually, no supercritical ORC has been designed yet, but they represent a realistic option for the near future.

However, an expansion similar to those of existing organic turbines is analyzed in **chapter 8**. The starting conditions are subcritical, and the real gas behavior of the fluid is seen to affect less the optimal solution than for the supercritical case, even though such influence is still relevent.

Then, **chapter 9** accounts for the viscous effects as well. After validating the flow solver over a flat plate, the formulation of the problem is rediscussed. In fact, while in the inviscid case the geometry can be rescaled afterwards to an arbitrary reference length, now the Reynolds number appears, which requires the choice of the reference length beforehand.

Finally, **chapter 10** draws some conclusions and shows the perspectives of the activity.

Chapter 2

The Organic Rankine Cycle

– I teach you all you need to know and then you go off to make a million dollars.

2.1 Overview

The concept of a heat engine using an organic working fluid is not new. The use of both biphenyl and phenyl ether in a binary cycle with water was proposed in the 1920s for powerplants. The first commercially available organic Rankine heat engine was marketed by Ormat Industries Ltd. (Yavne, Israel) in the early 1960s. It was designed to pump water for irrigation and the power level was about 1 kW_e.

In general, the ORC is a viable option from approximately 150 kW_e up to 2 MW_e, with major interests to the lower temperatures and lower power applications, for which they look far more attractive. These include solar energy, geothermal energy, waste heat recovery, and power generation for underwater or space applications. Some of the advantages of the ORCs may be resumed in the following [6]:

- heat is added to the cycle through an heat exchanger, making it relatively insensitive to the energy source;
- use of an appropriate working fluid allows the ORC to attain relatively high efficiency with simple single-stage turbomachinery even with moderate peak temperatures;

- working fluid properties frequently allow regeneration, increasing the Carnot efficiency;
- the moderate pressures and temperatures imply the use of conventional materials, long life, reliability and low maintenance cost.

2.2 Rankine Cycle Configurations

Referring to figure 2.1, the basic Rankine cycle engine consists of a feed pump, a vaporizer, a power expander and a condenser. Therefore, in the conventional cycle the fluid undergoes four successive changes: reversible adiabatic compression, pumping the liquid to the boiler; heating at constant pressure converting the liquid to vapor; reversible adiabatic expansion, performing work; cooling at constant pressure, condensing the vapor to liquid. The $T-s$ representation in figure 2.1 is typical for cycles employing steam as working fluid, which is the medium originally used by James Watt.

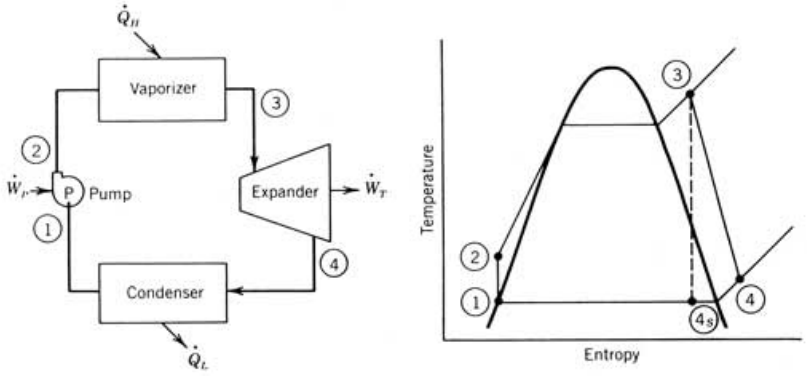

Figure 2.1: Configuration of a basic Rankine engine and its representation on the $T-s$ plane, from [7]

However, to efficiently apply the Rankine cycle for power generation with low-temperature heat sources (approximately from 70^oC to 400^oC) the working fluid must be an organic substance. In this case, the expansion phase is usually characterized by a low enthalpy drop, leaving a high temperature at the turbine exit and allowing the use of a regenerator to improve the cycle efficiency (figure 2.2).

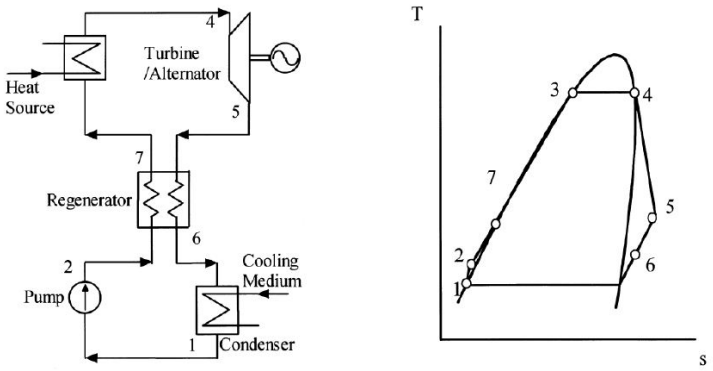

Figure 2.2: Configuration of a Rankine engine with regeneration and its representation on the $T - s$ plane, from [7]

So far, the largest part of ORC has been designed to operate at subcritical maximum cycle pressures. However, a so-called supercritical cycle further increases its efficiency, by increasing the average temperature of heat addition, as shown in figure 2.3. Given the condensation pressure and temperature, the increase in the maximum pressure implies a higher pump power consumption and a larger temperature (and enthapy) drop during the expansion, thus leading possibly to a multistage turbine. Moreover, the pump has to provide a bigger compression ratio, and the use of a single pump might lead to cavitation. Therefore two pumps may be necessary at the expense of higher investiment costs. Finally, the exploration of gas dynamics and heat transfer in supercritical organic fluids is at the beginning and currently the supercritical organic cycle is just a promising notion.

2.3 Working Fluids

The performance of a turbine is set by many factors, including blade profiles, but some dimensionless parameters based on the similarity rules are good indicators of its overall efficiency. The specific rotational speed N_s is one of them

$$N_S = n\frac{\sqrt{\dot{v}_{out}}}{\Delta h_{is}} \tag{2.1}$$

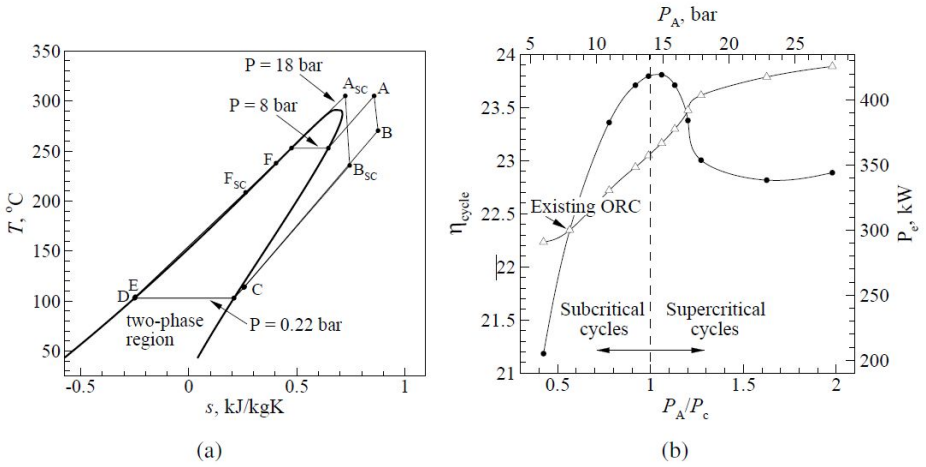

Figure 2.3: Supercritical and superheated cycle configuration on the left. Efficiency (•) and electric power output (△) as function of maximum pressure on the right, from [1]

where n is the dimensional rotational speed, $\dot{v}_{out}$ is the volumetric flow rate at stage outlet and Δh_{is} is the isentropic enthalpy drop.

From equation (2.1), to achieve the optimal N_S for a turbine with a high enthalpy drop, a high dimensional rotational speed n is needed. For low-power applications the flow rate is also small, and the results are excessive rotational speeds which increase both stage losses and blade stresses. Therefore, water is less suitable for low power applications because of the excessive Δh_{is} during the expansion with respect to an organic fluid. Moreover, steam density is also higher and leads to steam turbines with volumetric flow rates so small for low powers that the construction of the cycle components would not be feasable.

Therefore, organic turbines tend to operate at low peripheral speeds and small number of stages because of the lower enthalpy drop. Usually a small specific work is associated with a large expansion ratio (even over 100), so ORC turbines have to deal with supersonic flows and possible shock waves.

So, besides water, no other safe inorganic substance is suitable for Rankine cycles, which leaves endless possibilities in the field of organic substances. However, the field narrows rapidly when limitations and requirements are specified, for example:

- thermodynamic properties;
- chemical stability and compatibility with common materials of fabrication;
- non-corrosiveness, non-toxicity, non-flammability;
- ready availability;
- low cost.

If the system requirements have been determined, it is possible to define the optimum working fluid for that precise application. The most common problem is the lack of documentation regarding the thermodynamic properties of synthetized compounds. The most important parameter is the peak cycle temperature, which obviously requires the thermal stability of the fluid up to those conditions. Moreover, another importan aspect is the shape of the saturation curve. Contrary to water, most organic fluids suitable for power generation have a complex molecule and a "dry" saturation curve, which avoids the risk of condensation of the fluid during the expansion even without superheating (figure 2.4).

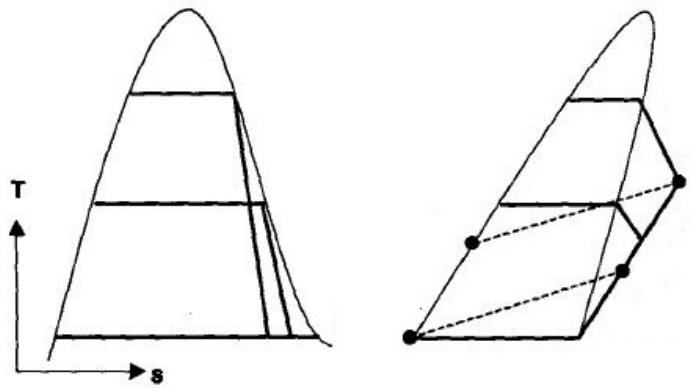

Figure 2.4: Saturation curves in the $T-s$ plane for water (left) and an organic compound (right), from [8]

Among the many substance suitable for ORC applications, hydrocarbons such as pentane, butane and toluene have to be remembered for their his-

torical importance, but have flammability concerns as well. Besides, perfluorocarbons exibit favourable critical parameters but are costly and their decomposition releases dangerous products (e.g. HF). Hydrofluorocarbons are a better fit the lower temperature applications (geothermal, heat recovery) due to their low critical temperature, but they have non-zero Global Warming Potential. More recent proposals regard the siloxanes, which are appropriate for the high temperature ORC (solar, biomass sources): they exibit zero Ozone Depletion Potential, almost zero Global Warming Potential, low toxicity, low flammablility and low cost.

To summarize, the adoption of an organic compound in place of water usually allows [2]:

- cycle configurations which are inaccessible with water, such as supercritical cycles even at low temperature and pressure;
- lower cycle maximum pressures;
- a better match between the heating trajectory of the working fluid and the cooling trajectory of the heat source;
- even for large source/sink temperature ratios, efficient thermodynamic cycles with simple layouts and a often single-stage expander;
- to avoid fluid condensation at the end of the expansion;
- their use as a lubricant for the turbine;
- the direct coupling of the turbine rotor with that of the electrical generator, due to the low rotational speeds;
- the design of optimum turbine sizes for a wide range of power levels.

2.4 The TROVA Facility

In order to overcome the lack of experimental data on flows representative of Organic Rankine Cycles turbine passages, a blow down wind tunnel for real gas applications has been designed and it is under construction at Laboratorio di Fluidodinamica delle Macchine (LFM) of Politecnico di Milano. The Test Rig for Organic Vapors [9] is a blow down facility aimed to characterize

organic vapor streams by means of independent measurements of pressure, temperature and velocity.

As shown in figure 2.5, the plant is provided with storage tanks and experiments cannot be continuous: the fluid under scrutiny, slowly vaporized in a high pressure vessel, feeds a test section at a lower pressure. The test section can be either a supersonic convergent-divergent nozzle or a turbine blade row. The exhausted vapor is collected and condensed in a low pressure tank; the loop is closed by liquid compression through a pump. Such operating system allows experiments on different operating conditions for a wide variety of working fluids, even though compounds for ORC applications (particularly Siloxanes and Fluorocarbons) remain of major interest. Depending on the fluid and boundary conditions, experiments may last from 20 seconds to several minutes.

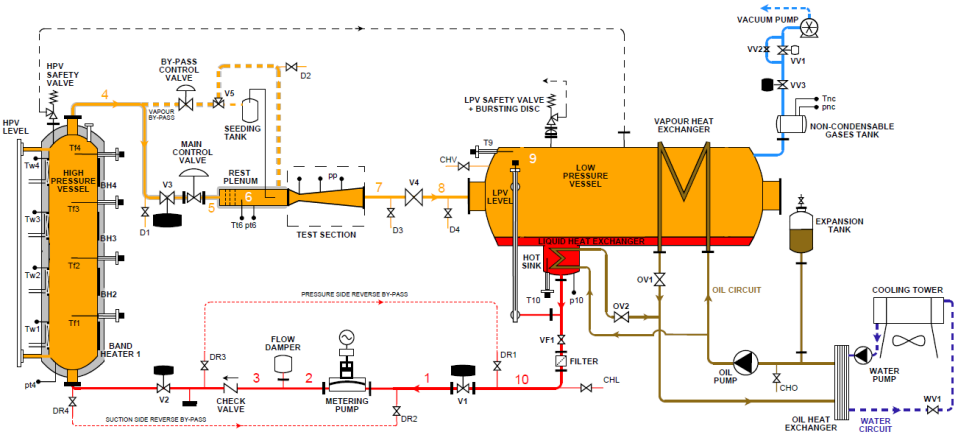

Figure 2.5: Sketch of the TROVA facility, from [9]

Although expansions occurring through ORC turbine blade passages are the main research interest, the test rig is initially equipped with a straight axis convergent-divergent nozzle. It performs a quasi-1D expansion, regarded as the simplest stream representative of ORC turbomachinery passages flow field.

The characterization of the real gas expansion can be performed by the upstream measurement of total pressure and total temperature. Along the expansion line, the contemporary direct measurement of static pressure and velocity complete the investigation. Visualization of supersonic flow patterns

can be arranged by Schlieren technique. In order to easily perform optical measurements along the expansion line, a rectangular cross section nozzle mounting a glass window has been chosen.

Chapter 3

Dense Gas Flows of Organic Fluids

– All fighters are pig headed someway or another, some part of them always thinks they know better than you about something.

3.1 Overview

Hydrocarbons, fluorocarbons and siloxanes in ORC power plants are often used in conditions close to the critical point. Table 3.1 resumes the critical conditions, as well as the molecular masses and the chemical formulas of candidate working fluids. While for low reduced pressures and high reduced temperatures the ideal gas law is a good and simple approximation of the real behavior of the fluid, for thermodynamic states close to the critical point (approximately $0.9 < P/P_c < 1.2$ and $0.8 < T/T_c < 1.3$) molecular interactions have to be taken into account in modeling the fluid and the ideal gas law becomes inappropriate.

Such differences can be resumed as a volumetric effect and a calorimetric effect [10]. The former implies that the $P - v - T$ relation of dense gases is different from that of a perfect gas: in fact specific volumes are smaller if compared to the ideal approximation, see figure 3.1. The latter implies that

Table 3.1: Chemical formulas, molecular masses and critical values of candidate organic fluids

	Chemical formula	$M\ (g/mol)$	$T_c\ (K)$	$P_c\ (atm)$
Fluorocarbons				
PP5	$C_{10}F_{18}$	462	565.2	17.3
PP10	$C_{13}F_{22}$	574	630.2	16.2
Hydrocarbons				
toluene	C_7H_8	92.1	591.8	40.7
decane	$C_{10}H_{22}$	142.3	617.7	20.7
Siloxanes				
MD_4M	$C_{14}H_{42}O_5Si_6$	459	653.2	8.0
D_5	$C_{10}H_{30}O_5Si_5$	371	619.1	11.4

the heat capacity close to critical point tends to large values [10]:

$$C_v(v,T) = C_v^0(T) + T\int_\infty^v \left(\frac{\partial^2 P}{\partial T^2}\right)_v dv \tag{3.1}$$

where $C_v^0(T)$ is the specific heat in the ideal-gas limit. The contribution of the integral in equation 3.1 vanishes for the ideal (politropic or non-politropic) gas, because of the degenerate nature if its equation of state $Pv = RT$. Moreover, figure 3.2 shows the difference in the shape of the isentrope curves between the ideal gas approximation and the real gas. The slope of the isentrope in the $P - v$ plane is directly the speed of sound, which is quite a relevant factor in gasdynamic problems.

3.2 Nonclassical Gasdynamics

The influence of molecular complexity has on the speed of sound trend is found to have deep implications on the gasdynamic behavior of the fluid. In particular, such gasdynamic behavior is in a strong relation to the fundamental derivative of gasdynamics, defined as [11]

$$\Gamma = 1 - \frac{v}{c}\left(\frac{\partial c}{\partial v}\right)_s \tag{3.2}$$

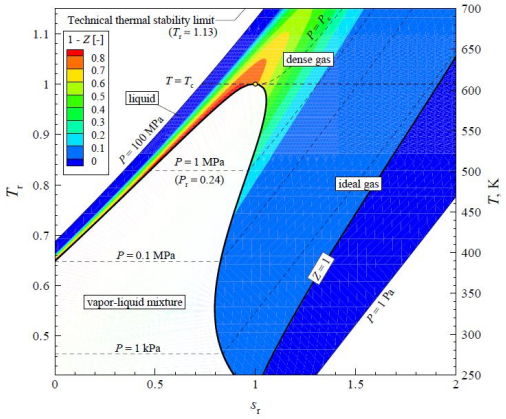

Figure 3.1: Deviation from ideal gas, volumetric effect. Compressibility factor in the reduced temperature-entropy diagram of toluene, from [1]

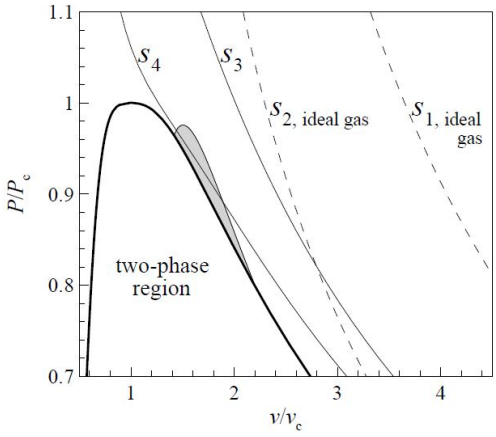

Figure 3.2: Deviation from ideal gas, calorimetric effect. Isentrope curves for D_6, from [1]. Correct isentrope from ideal gas model s_1, wrong prediction of the ideal gas model in the dense gas region s_2, correct curve for dense gas s_3, and BZT behavior along s_4

Even the relatively simple van der Waals model [12] is sufficient to highlight that complex molecules in conditions close to the critical point may exibit values of the fundamental derivative less than unity, namely having the the speed of sound dependence on the density reversed with respect to the ideal gas (figure 3.3). This usually leads to classical gasdynamic phenomena, but if Γ becomes negative, nonclassical phenomena are admissible such as rarefaction shocks or isoentropic compressions. Fluids who exibit the nonclassical phenomena over a finite range of temperature and pressure are referred to as Bethe-Zel'dovich-Thompson (BZT) fluids after the authors who made the first studies in the field.

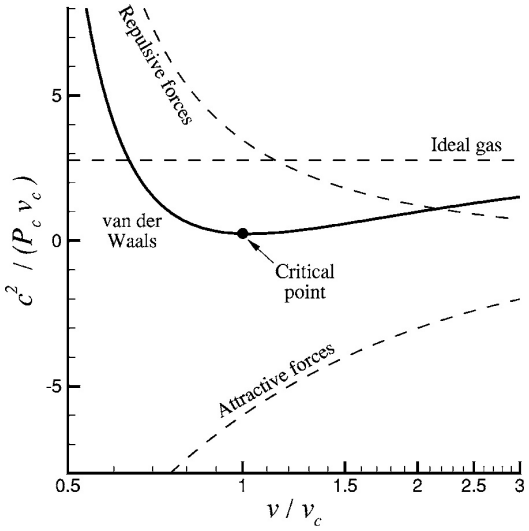

Figure 3.3: Sound speed variation along the critical isotherm compared to the ideal gas. Effects of attractive and repulsive forces are also shown, from [12]

Gasdynamic behavior relation to the fundamental derivative can be summarized as follows [11]:

- $\Gamma > 1$, classical (ideal gas) behavior, soundspeed increases with density;
- $\Gamma = 1$, classical (non ideal) behavior, soundspeed is constant with density, pressure is a linear function of density;

- $0 < \Gamma < 1$, classical (non ideal) behavior, soundspeed decreases with density;
- $\Gamma = 0$, pressure is a linear function of specific volume;
- $\Gamma < 0$, nonclassical behavior.

From this viewpoint, a correct estimation of the fundamental derivative is crucial for a correct estimation phenomenological behavior of the flow. However, the extention of the negative-Γ region are strongly influenced by the thermodynamic model adopted, sometimes happening that a model admits the existence of that region while another does not (see [13] for some examples).

3.3 Thermodynamic Models

It has been shown that even a simple non ideal gas model can display the features typical of the real gas. However, its accuracy is still low and many other thermodynamic models are availabe to compute the fluids' properties more accurately. There exist different levels of sophistication, each of them acceptable depending on the problem. In any case the model has to be consistent to achieve robustness and accuracy: all the thermodynamic properties have to be computed from the minimum set of information, usually a relation for the pressure in the form $P = P(v, T)$ and another for the heat capacity in the ideal gas state as function of the temperature $C_P^0 = C_P^0(T)$.

A first class of thermodynamic models requires only the critical parameters and the acentric factor of the fluid to define the $P - v - T$ relation. For example, the cubic Peng-Robinson-Stryjek-Vera equation of state (EoS) has the form:

$$P = \frac{RT}{v - b} - \frac{a(T)}{v(v + b) + b(v - b)} \tag{3.3}$$

in which the aforementioned parameters enter in the definition of a and b, the contributions of the attractive and repulsive intermolecular forces respectively. Compared to the well-known polytropic ideal gas EoS, the PRSV EoS allows for better predictions in the dense gas region, even though not so accurate close to the critical point ($P/Pc > 0.9$).

More accurate thermodynamic models are the so-called multiparameter EoS. An example can be found in the Span-Wagner EoS, suitable for non-polar and weakly polar fluids. This state-of-the-art EoS features the reduced Helmholtz energy $\psi = \Psi/RT$ as a function of the reduced density, $\delta = \rho/\rho_c$ and the inverse of the reduced temperature $\tau = T_c/T$. It overcomes the deficiencies of the cubic Eos being extremely accurate also in the vicinity of the critical point and has an excellent numerical stability compared with older multi-parameter EoSs. For instance, the equation's 12 parameters can easily be determined from a restricted set of experimental measures, an important feature when facing the limited amount of experimental data present in literature. Furthermore, due to its particular functional form, it returns realistic predictions with a limited number of parameters, even for extrapolations outside the range of availability of experimeltal data.

A polynomial expression for the ideal gas specific heat C_P^0 is often sufficient for every EoS.

3.4 CFD Simulations

The software which will be used for the fluid dynamic simulation is zFlow, a code developed primarily to solve the Euler equations for fluids in the classical dense gas and nonclassical regime [14]. The spatial approximation of the Euler equations is constructed with an high resolution finite volume method suitable for general unstructured and hybrid grids, allowing the straightforward treatment of domains of arbitrarily complex geometry. Based on the works by Selmin [15] and Selmin and Formaggia [16], the implemented procedures can be regarded as an hybrid between the finite element (FE) and finite volume (FV) methods. In fact, the finite volume metric quantities are constructed on the basis of the Lagrangian polynomial shape functions typically used in finite element methods, making this type of FV schemes with a centred numerical flux function identical to a classical FE discretization. The high-resolution upwind discretization is constructed on the basis of the Roe approximate Riemann solver generalized to the case of fluids characterized by arbitrary equations of state according to Vinokur and Montagné [17]. This class of discretization schemes is particularly well suited to the computation of high Mach number flows such as those occurring in an ORC turbine.

Furthermore, in zFlow are implemented both explicit and implicit time

integration schemes, being the implicit much more efficient when facing steady-state solutions. Improving the time integration efficieny is crucial when the the CFD code has to use complex thermodynamic models which tend to slow down the single time advance. zFlow interacts with FluidProp [18], a state-of-the-art thermodynamic library for the calculation of properties of pure fluids and mixtures, beyond the model of ideal gas.

Finally, a recent extension of the code allows for the solution of the Reynolds-averaged compressible Navier-Stokes (RANS) equations coupled with a non-standard implementation of the high- or low-Reynolds number $k-\omega$ turbulence model to favor numerical stability [19].

Chapter 4

Nozzle Geometry Optimization Strategy

– That's the stupidest thing I've ever heard of, how the hell we gonna do that?

4.1 Definition of an Optimization Problem

The development of computational power during the last decades allowed the use of numerical tools such as CFD with a high level of reliability, performing the desired analysis in a reasonable amount of time, ranging from several minutes to a few days. In this view, the new challenge for the designer is to evaluate and compare many different configurations in order to find the one that fits best his requirements, the optimum design.

As in all optimization problems, there are three points which should be made clear at the beginning and which determine a large part of the final result: the definition of performances (the objective function) representative of the quality of the system, the choice of the indipendent variables and the constraints which may limit the range of search [20]. For example, the chioce of a set of independent variables may lead sooner to a better optimum than another set of variables.

Optimization problems can be divided into single- and multi-objective, depending on the number of the functions to be optimized. In general, a

multi-objective problem is stated as following:

$$\begin{array}{ll} \min f_i(\mathbf{x}) & i = 1 \dots l \\ g_j(\mathbf{x}) \leq 0 & j = 1 \dots m \\ h_k(\mathbf{x}) = 0 & k = 1 \dots n \\ x_p^l(\mathbf{x}) \leq x_p \leq x_p^u(\mathbf{x}) & p = 1 \dots q \end{array} \tag{4.1}$$

where $\mathbf{x} = (x_1 \dots x_q)^T$ is the vector of design variables. So, the optimization problem (4.1) translates into minimizing a set of objectives $f_i(\mathbf{x})$, possibly subject to constraints $g_j(\mathbf{x})$ or $h_k(\mathbf{x})$, and with the search range limited by the last relation of (4.1).

Common engineering applications that involve the maximization of a performance (such as efficiency) can be turned into a minimization problem by taking the inverse value. In case of multi-objective optimizations, the objectives often conflict one another (for example maximizing the strength of a component while minimizing its weight) and does not exist a unique value of $\mathbf{x}$ solution of (4.1). The so-called Pareto front analysis is a method to identify a set of dominant solutions, such as in figure 4.1. However, when facing 4 or more objectives, the visualization of the front becomes less immediate, so that fewer objectives are often preferable. This can be achieved by choosing an appropriate set of weights w_i and combining some of the objectives into a single function:

$$F(\mathbf{x}) = \sum_{i=1}^{l} w_i f_i(\mathbf{x}) \tag{4.2}$$

Finally, two aspects need remarking. Firstly, the optimization process involves a tradeoff between the computational effort (efficiency) and the value of the optimum (effectiveness). Secondly, although the attainment of the absolute optimum is the goal of any algorithm, the most important goal of optimization is improving the current state.

4.2 Optimization Methods

In the research for the optimum, a sistematic sweep of the design space is not feasable: supposing there are v values of the n design parameters, v^n functional evaluation are required. With both parameters of the order of 10 and accounting for the time of every single analysis, this way is definitely too

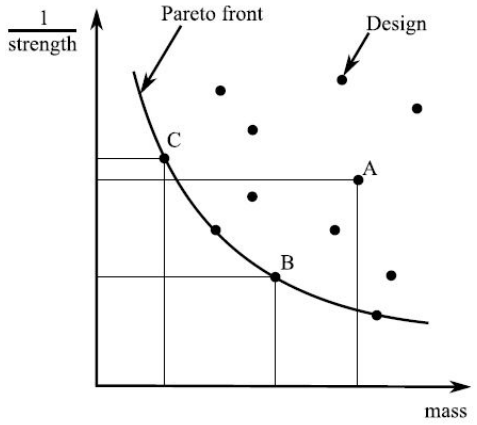

Figure 4.1: Typical Pareto front for a 2-objective optimization problem. Design A is dominated by design B, but design B and C do not dominate each other

expensive. Past decades have seen a large development of efficient optimization algorithms, which are allowed to modify the design parameters in order to maximize its performance.

Currently, there is a wide variety of methods available. They can be subdivided depending on the order of derivatives of the objective function used. For example, zero order methods use only the function values in their search for the minimum, while first and second order methods use respectively the first and second order derivatives. Zero order methods are ganerally more expensive in term of computer resources because they require a larger number of function evaluation (so, a larger number of analysis), but never get stuck in a local optimum. On the other hand, superior order methods require less function evaluations but need the computation of the gradients as well, which is no easy task, and they risk to converge on a local optimum. For these reasons, zero order methods seem the most reliable option in terms of the outcome.

For fluid dynamic applications there are examples adopting efficient Genetic Algorithms (GA) zero order methods. GAs are based on the mechanisms of natural selection to obtain the optimum. They start with an initial population in which each individual is represented by a binary string containing all the values of the parameters. The total length of the string depends from

the number of parameters representing the individual and from the number of bits dedicated to each parameter (the substring length, which stands for the accuracy desired). It has to be taken into account that an extremely accurate representation leads to a slow convergence to the optimum, while a scarce resolution leads to a worse optimum configuration: for example it has been reported that a substring length of 8 bits was the ideal value for the optimization of the 3D radial turbine reported in [21].

From the initial population the GA, based on a mix of both random choice and fitness indicators, selects couples of individuals to build successive generations. The two individuals selected as parents reproduce by the so-called crossover: the binary strings are recombined at a randomly chosen position generating two new individuals, the offspring. Besides crossover reproduction, also a mutation mechanism is used: this process changes a bit in the binary sequence of the original state after the crossover. The mutation allows the algorithm not to be trapped in a local minimum. By setting the criteria of selection of the parents, the crossover and mutation probability, the speed to converge to the optimum can be altered. The GA mechanisms are resumed in figure 4.2.

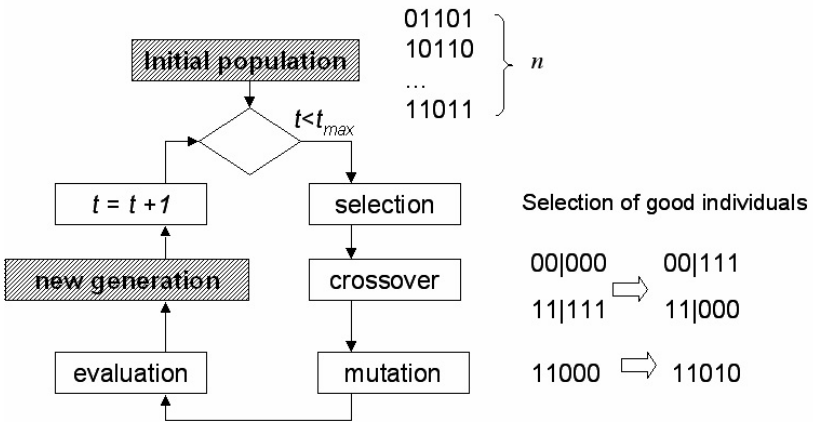

Figure 4.2: Working principle of the Genetic Algorithm

During the evolutionary process, it is possible that the best individual is lost by mutation or crossover. To prevent this loss of valuable information, most GAs use the elitism strategy. In case the best individual of the new generation is worse than that of a previous generation, the latter one will

replace a randomly selected individual of the new generation. However, the computational effort required is still too high because the GA needs a population sufficiently large and enough generations to converge to the optimum, which imply too many expensive analysis are necessary.

The present work makes use of the commercial software modeFrontier, a multipurpose optimization environment which implements all these procedures.

4.3 Surrogate Models in Genetic Algorithms

To obtain better time performance without altering the quality of the final result, faster but less accurate models can be used in place of many direct evaluations. Such models (often referred to as surrogate or metamodels) have already been applied for fluid dynamic analysis and design [22], [1]. Given a generic individual $\mathbf{x}$ with the i-th performance being $f_i(\mathbf{x})$, the surrogate is a function $\widetilde{f}_i(\mathbf{x})$ such that

$$\left|\left|\widetilde{f}_i(\mathbf{x}) - f_i(\mathbf{x})\right|\right| < \epsilon_i \tag{4.3}$$

with ϵ_i sufficiently small.

The surrogate has no relation to the physical phenomenum and bases his knowledge on a database to quickly estimate the quality of a candidate design $\mathbf{x}$. The metamodel has a some coefficients inside each $\widetilde{f}_i$ that need to be adapted to make $\widetilde{f}_i$ a valid substitute for f_i during the optimization: this is the training process. A set of cases is analyzed with the highly accurate model so that a series of input/output relations is known. Then, the metamodel's parameters are tuned to maximize the accuracy on those samples and now the surrogate becomes able to make predictions also for other individuals. If the training set is chosen wisely, the metamodel can extract the maximum amount of information with little effort.

In any case, the two-level interaction allows the metamodel to adjust its parameters during the optimization process even for a bad initial training. In fact, the training database can be refined computing with the CFD solver the more promising individuals according to the metamodel, in order to improve its accuracy in the more promising directions. Figure 4.3 resumes the optimization strategy just described.

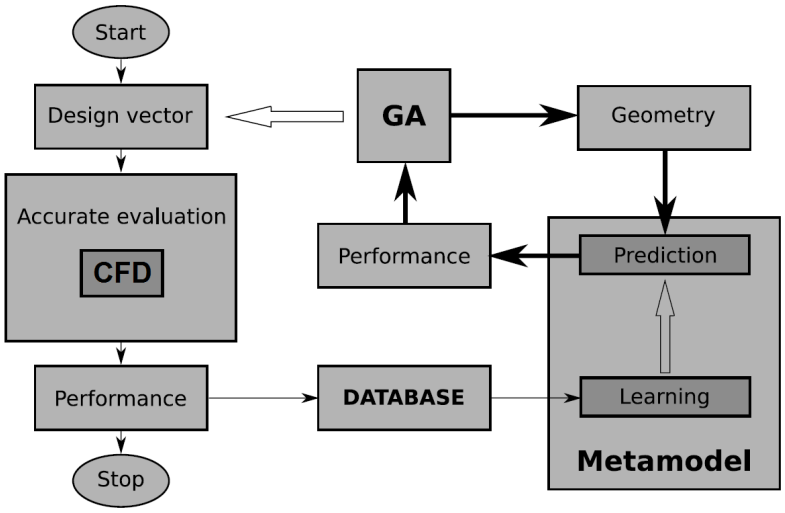

Figure 4.3: Flowchart of optimization system, retrieved from [22]. The scheme shows the CFD solver, the metamodel and their mutual interaction through the Genetic Algorithm

Surrogate models differ from each other by assuming different structures for $\widetilde{f}_i$. The software modeFrontier allows a choice between many types of metamodels, even though not each of them is suitable for fluid dynamics applications. At the end, the selection of the most appropriate metamodel is done directly by selecting a test set of $\mathbf{x}$, by evaluating exactly their outputs $f_i(\mathbf{x})$, and by comparing it with the prediction of the metamodel $\widetilde{f}_i(\mathbf{x})$ as in equation 4.3. However, some general guidelines direct the initial research. For instance, a polynomial approximation of the output functions is not prone for fluid dynamics problems, because it is not expected any linear, quadratic, or cubic trend between the input variables and the outputs. Similarly, the statistical models that require a large number of training samples seem inappropriate: regardless of their accuracy, the preparation of the training database would be too expensive. Therefore, the focus shifts towards those models able to make predictions from a limited training database, and whose structure allows to account for the high non-linearity of the CFD problem. In the following, a brief description of some promising metamodels is given.

4.3.1 Artificial Neural Networks

Although Artificial Neural Networks (ANN) were initially designed to imitate certain brain functions (character recognition, voice recognition, image processing, etc), they can also be used as interpolators. Figure 4.4 gives a schematic view of an ANN: elementary process units (the neurons) are arranged in layers and joined by connections of different intensity to form a parallel architecture.

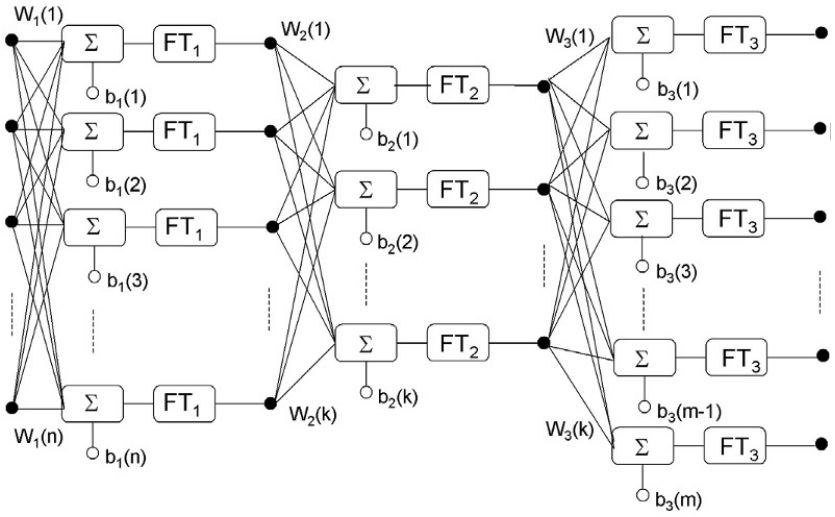

Figure 4.4: Artificial Neural Network with one hidden layer

Each element of the first input layer is connected to each neuron of the first hidden layer. Suppose the ANN has n input variables $\mathbf{x} = (x_1 \dots x_n)^T$ and one hidden layer with h hidden neurons. The input given to the k-th neuron of the hidden layer is given by

$$in_k^{\text{HID}} = \sum_{p=1}^{n} w_{p,k}^{\text{HID}} x_p + b_k^{\text{HID}} \tag{4.4}$$

where the $w_{p,k}^{\text{HID}}$ are the connection weights and the b_k^{HID} the bias given each neuron. Then, to every neuron is associated a transfer funcition, for example

$$out_k^{\text{HID}} = FT(in_k^{\text{HID}}) = \frac{1}{1 + \exp(-in_k^{\text{HID}})} \tag{4.5}$$

Finally, the output of the network is computed as

$$\widetilde{f}_i = FT\left(\sum_{k=1}^{h} w_{k,j}^{\text{OUT}} out_k^{\text{HID}} + b_j^{\text{OUT}}\right) \tag{4.6}$$

where other weights and other bias come into play.

4.3.2 Radial Basis Functions Networks

Radial Basis Functions (RBF) networks belong to the same class as ANN, however they have a different architecture and input to output relation. Figure 4.5 shows the architecture of a RBF network for a 2-dimensional input and one hidden layer. In general, each hidden neuron j has a n-dimensional input $(x_1 \dots x_n)$ and vector $\mathbf{c}_j \in R^n$, which is the center of a nonlinear radial basis function $h : R^n \to R$. This activation funciton is proportional to the distance of the input vector $\mathbf{x}$ to the center $\mathbf{c}_j$:

$$h_j(\mathbf{x}) = g_j(||\mathbf{x} - \mathbf{c}_j||) \tag{4.7}$$

where is usually the Gaussian function determined by the amplitude σ_j:

$$g_j(||\mathbf{x} - \mathbf{c}_j||) = \exp\left(-\frac{||\mathbf{x} - \mathbf{c}_j||^2}{\sigma_j^2}\right) \tag{4.8}$$

The closer $\mathbf{x}$ is to the center $\mathbf{c}_j$, the higher the output of the activation function will be. The network output is obtained as the weighed sum of all responses of the hidden layer:

$$\widetilde{f}_i = \sum_{j=1}^{h} w_{i,j} h_j(\mathbf{x}) + b_i \tag{4.9}$$

4.3.3 Kriging

Kriging was initially developed by geologists to estimate mineral concentrations over an area of interest given a set of sampled sites from that area. Successively, the model was extended to a generic n-dimensional inputs, whereas geostatistics considers only two-dimensional inputs.

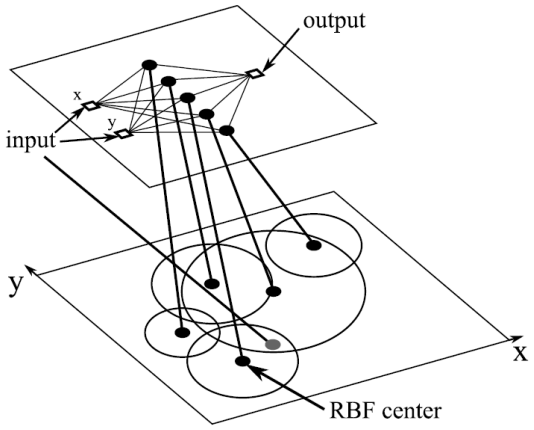

Figure 4.5: A 2D RBF network, with the position of RBF centers in 2D space. From [22]

Kriging belongs to the family of linear least squares algorithms. However, it is able to reproduce the observed data exactly ($\widetilde{f}_i(\mathbf{x}^{\text{OBS}}) = f_i(\mathbf{x}^{\text{OBS}})$), which represents a major advantage over the other metamodels. The mathematical form of Kriging consists of two parts:

$$\widetilde{f}_i(\mathbf{x}) = \sum_{j=1}^{k} \beta_j g_j(\mathbf{x}) + Z(\mathbf{x}) \tag{4.10}$$

with a linear regression of the functions $g_j(\mathbf{x})$ to catch the main trend of the response and $Z(\mathbf{x})$, a model of Gaussian stationary random process with zero mean. An assumption is made on the mathematical form of the covariance of $Z(\mathbf{x})$, which is usually a Gaussian function. The parameters β_j and the function $Z(\mathbf{x})$ are determined such that $\widetilde{f}(\mathbf{x})$ is the best linear unbiased predictor. A linear estimator means that $\widetilde{f}(\mathbf{x})$ can be written as a linear combination of the N observation samples:

$$\widetilde{f}_i(\mathbf{x}) = \sum_{k=1}^{N} w_k(\mathbf{x}) f_i(\mathbf{x}_k) \tag{4.11}$$

So, if $\mathbf{x}$ is an observed value (namely if $\mathbf{x} = \mathbf{x}_i$), then

$$w_k(\mathbf{x}_i) = 0 \quad \text{for} \quad k \neq i \tag{4.12}$$

$$w_k(\mathbf{x}_i) = 1 \quad \text{for} \quad k = i \tag{4.13}$$

which makes the Kriging is an exact predictor on the observed points. A more detailed review of the Kriging model can be found in [23].

Chapter 5

Definition of Nozzle Geometry

– You're in a position to negotiate?

5.1 Introduction

The analysis of expansions occurring through ORC turbine blade passages are the ultimate interest of the work. However, for a preliminary evaluation of the real gas effects, a simpler geometry is equally acceptable. Therefore a two dimensional converging-diverging nozzle is enough to reproduce an expansion similar to that of ORC turbines in terms of pressure ratios and discharge Mach number.

So, a nozzle with rectangular cross-sectional area is considered, so that the flowfield is symmetric with respect to the x axis. The present task is to describe the solid wall geometry with the least set of parameters, which should allow at the same time sufficient flexibility to represent a wide variety of configurations. The present parametrization has been taken from Pasquale [5].

5.2 Parametrization

Two categories of parameters are employed to describe the solid wall. The first one defines the general dimesions of the nozzle (lengths and areas), while the second one gives the accurate description of the wall.

5.2.1 Macroparameters

The geometry of the upper half of the nozzle is shown in figure 5.1. The fluid enters from the left boundary and exits from the right one, while the lower boundary is the axis of symmetry and the upper boundary the solid wall.

The total length of the nozzle is fixed to one and the only other dimensional parameter is the throat area S_t. The other quantities are all scaled to the throat area:

- inflow area $S_i = s_i S_t$
- inlet length $L_i = l_i S_i$
- outflow area $S_o = s_o S_t$
- throat location $L_c = l_c S_t$
- throat curvature $C_t = c_t S_t$

in which the lower case nondimensional parameters are the variables of the problem. The fixed total length is not a limiting factor because the inviscid problem can be formulated either as a minimization of nozzle length for constant throat area, or equivalently as a maximization of the throat area for a fixed total length. In fact, a simple rescaling of figure 5.1 brings figure 5.2, which shows a fixed throat and a variable length. In the inviscid case the rescaling does not affect the solution, while for the viscous calculations the reference length influences Reynolds number. This problem will be discussed later.

Moreover, figure 5.2 shows that fixing s_i, l_i and l_c freezes the converging, so that the parametrization allows also for diverging-only optimizations.

The aforementioned parameters are subject to some constraints. The throat location must not exceed the total nozzle length, while the inflow and outflow areas have to be greater than the throat. The straight duct added upstream of the nozzle inlet aims to reduce the influence of the inflow boundary condition on the solution, therefore it can be reasonably assumed $l_i = 1$.

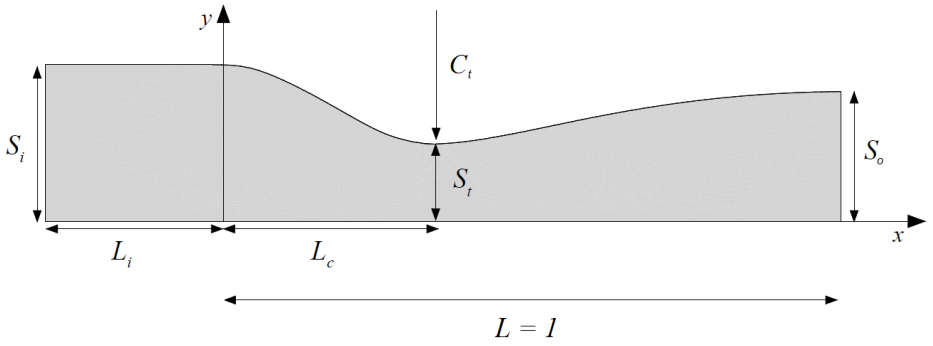

Figure 5.1: Upper half of the nozzle geometry with a rectangular cross-sectional area

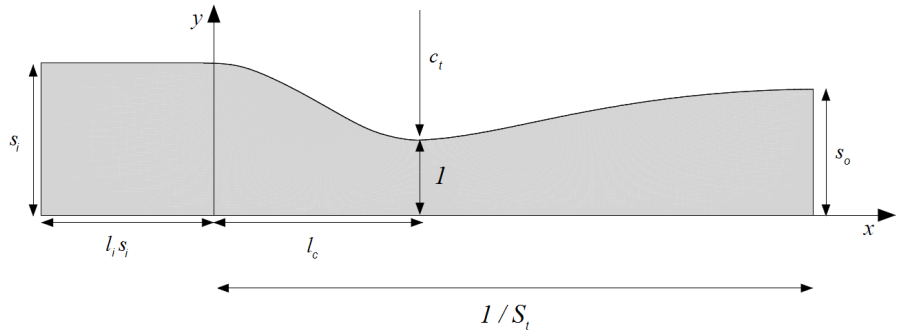

Figure 5.2: Upper half of the nozzle rescaled to unitarian throat section

5.2.2 Accurate Wall Description

The converging-diverging wall shape of the nozzle is represented by cubic B-spline curves, which are briefly presented in the following.

A B-spline curve $\mathbf{B}(u)$ of degree p can in general be written as

$$\mathbf{B}(u) = \sum_{i=0}^{n} N_{i,p}(u)\mathbf{P}_i \tag{5.1}$$

where $\mathbf{P}_i$ is one of the $n+1$ control points and $n \geq p$, $N_{i,p}$ are the basis functions. The parameter u varies on the interval $[u_0, u_m]$, where u_0 and u_m are the first and last elements of a strictly increasing sequence of $m+1$

knots. The number of control points, the degree of the curve and the number of knots are related one another by the relation

$$m = n + p + 1 \tag{5.2}$$

For example, for a cubic B-spline ($p = 3$) the minimum number of control points is $n+1 = 4$ and the corresponding number of knots is $m = n+p+1 = 8$.

To completely define a curve, the knot sequence also has to be fixed. In general, for a given set of control points, it is difficult to judge which knot sequence is the best choice. The easiest option is to choose a uniform spacing, which is however too rigid in many cases. As a rule of thumb, better results in terms of curve smoothness are obtained if the control point location is somehow reflected in the knot sequence. In this work the knot sequence is computed by a chordal parametrization.

In this work the solid wall of the nozzle is represented as a composition of two consecutive cubic B-spline curves. The first curve $\mathbf{B}_c(u)$ is used for the converging part and it ends at the throat area location $T = (L_c, S_t)$. The other curve $\mathbf{B}_d(u)$ represents the diverging part. These curves are defined by n_c+1 and n_d+1 number of points respectively, and the shape of the upper wall is controlled by the position of the control points for both curves. Moreover, at the throat location, a fixed curvature value can be imposed preserving the C^2 continuity between the two curves if some additional constraints around the junction point are satisfied. In the case of cubic curves, these conditions concern only the two adjacent control points and the spacing of the first two different knots for both curves.

The shape of both the converging and diverging walls is controlled by the position of the unconstrained control points $\mathbf{P}_i = (x_i, y_i)$, each represented by two parameters ξ_i and η_i. Such parameters vary in the interval $[0, 1]$ and represent the dimensionless distance from the known points (inflow, throat and outflow), namely for the converging part

$$\begin{aligned} x_i &= \xi_i L_c \\ y_i &= S_t + \eta_i (S_i - S_t) \end{aligned} \tag{5.3}$$

and similarly for the diverging part. So, even though might happen $y_i = S_t$ for some control points, the minimum flow passage is always at the throat location because the B-spline does not pass on the control points. Figure 5.3 shows a couple of examples of geometries obtainable.

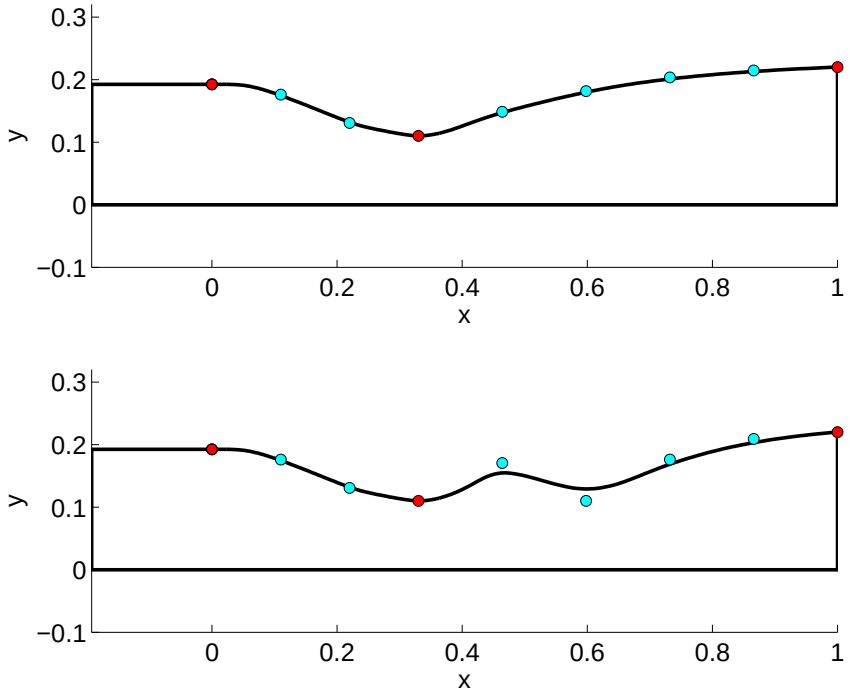

Figure 5.3: Example of geometries generated with the present parametrization, location of the global points (red) and location of the control points (blue)

5.3 Test Geometry

The test geometry of figure 5.4 is considered to evaluate the capabilities of the present parametrization. Such figure shows a two dimensional nozzle designed with the Method of Characteristics featuring MDM as working fluid [24]. That design is carried out with an accurate thermodynamic model for the fluid which accounts for real gas effects.

Now, the goal is to accurately reproduce that geometry with the parameters introduced in this chapter. However, the MoC design neglects the converging part, since the characteristic lines exist only in the supersonic

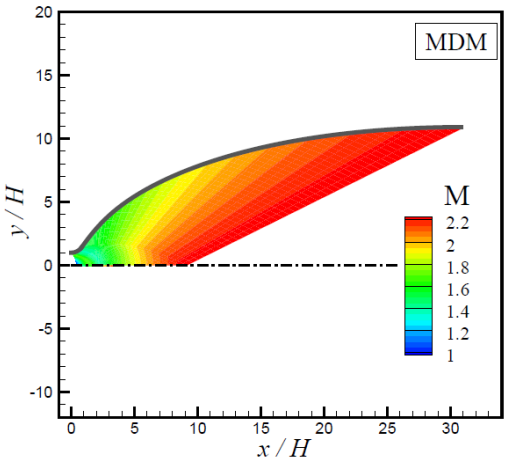

Figure 5.4: Reference geometry and Mach number distribution according to the Method of Characteristics, from [24]

region[1], so the comparison can be made only for the diverging part.

Firstly, the throat section S_t and the converging length l_c are fixed in order to achieve the same length for the diverging part. Then, every parameter related to the converging part is arbitrarily assumed. That leaves the throat curvature c_t, the outflow section s_o, and the position of n_d control points for the diverging part to be adjusted to the reference geometry.

In principle, the control points can be moved along both the (x, y) coordinates by ruling the dimensionless parameters (ξ, η). However, their x components are fixed according to arbitrarily imposed relations. For example, the abscissa of the i-th control point can be placed according to a linear or a cosine distribution

$$\xi_i = \frac{i}{n_d + 1} \tag{5.4}$$

$$\xi_i = 1 - \cos\left(\frac{\pi}{2}\frac{i}{n_d + 1}\right) \tag{5.5}$$

so that

$$x_i = L_c + (1 - L_c)\xi_i \tag{5.6}$$

[1]The MoC design starts from an approximate solution at the throat, such as the one by Sauer [4]

Then, the variance of the resulting B-spline to the reference geometry is minimized with respect to the remaining variables η_i, c_t and s_o. Figure 5.5 shows the results depending on the number of control points n_d. The cosine distribution is able to approach the reference even with a limited number of parameters and increasing the number of control points does not lead to substantial improvements. On the other hand, the linear distribution benefits from increasing the number of free variables although it never reaches the same accuracy as the cosine distribution.

In this way, the reference geometry can be recovered with the desired level of accuracy.

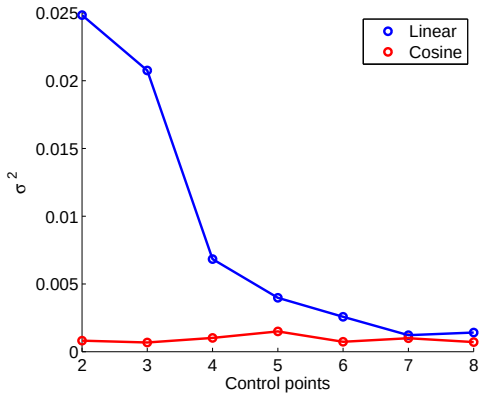

Figure 5.5: Variance of the B-splines with increasing number of control points, with respect to the reference geometry. The linear and cosine x-distributions correspond to equations (5.4) and (5.5) respectively

Chapter 6

Optimization of an Ideal Gas Nozzle

– Don't you say that, don't you say that if it ain't true!

6.1 Introduction

The present chapter applies the notions presented in chapter 4 to find the optimal shape of a 2-D axial nozzle. The the criteria for the optimum and the choice of the design variables will be explained in details, but first a working fluid needs selecting.

As mentioned in chapter 2, the siloxanes represent one of the most attractive options for ORC applications: they have zero Ozone Depletion Potential, very low Global Warming Potential and low cost. Even if they operate in proximity of their thermal stability limit, their decomposition releases non-toxic compounds. In this view, the compound selected is MDM, whose main properties are reported in Table 6.1. Moreover, MDM is currently used in many ORC plants, in which the flow can be accelerated to supersonic conditions around $M = 2.2$ at the end of the turbine stator. Therefore, that Mach number represents also the designed discharge conditions for the two dimensional nozzle under examination.

Assuming a politropic ideal-gas model for the fluid, the absolute thermodynamic conditions are neglected, since the relevant parameters are the

Table 6.1: Main properties of MDM

Complete Name	Octamethyltrisiloxane
Chemical Formula	C_8 H_{24} Si_3 O_2
MM	236.5 $kg/kmol$
T_c	290.94 ^oC
P_c	14.15 bar
ρ_c	273.86 kg/m^3

ratios. For example, according to the isentropic relations [4] is

$$\frac{P_e}{P_0} = \left(1 + \frac{\gamma - 1}{2} M_e^2\right)^{\frac{\gamma}{1-\gamma}} \tag{6.1}$$

so that the discharge pressure P_e can be rescaled (afterwards and without consequences) to an arbitrary reference value P_0 for the same outflow Mach number M_e and specific heat ratio γ.

The only two parameters ruling the behavior of the fluid in the politropic ideal-gas case are the specific gas constant R and the heat capacity ratio γ. The former is the ratio between the universal gas constant and the fluid molar mass, while the latter can be calculated from the number of active degrees of freedom N as

$$\gamma = 1 + \frac{2}{N} \tag{6.2}$$

In the dilute gas limit, the MDM features $N = 115$ [1], which leads to $\gamma = 1.017$.

To have a preliminary idea of the dimensions of the nozzle, a simplified approach allows to calculate the throat-to-exit area ratio as function of the discharge Mach number and the heat capacity ratio. According to the one-dimensional isentropic relations [4]

$$\frac{S_e}{S_t} = \frac{1}{M_e}\left[\frac{2}{\gamma + 1}\left(1 + \frac{\gamma - 1}{2} M_e^2\right)\right]^{\frac{\gamma+1}{2(\gamma-1)}} = 3.008 \tag{6.3}$$

Now the discussion aims to build up thoroughly the optimization.

6.2 Objectives

The desired characteristics of the optimal nozzle involve different aspects which can be resumed as:

- uniform flow at nozzle exit;
- outflow angle at nozzle exit;
- dissipation within the nozzle;
- minimal nozzle length.

The first two targets can be treated together, since they concern either the absolute Mach number and the flow angle, or the two components of the Mach number: here is preferred the former formulation which allows for a more immediate visualization of the two aspects, for example in the choice of the relative weigths which will be discussed later. As for the dissipation within the nozzle which is evaluated with the total pressure at the outflow, it is treated as a constraint. In fact, if considering the total pressure loss in the objectives means a penalty for the shock-affected geometries (so that the Genetic Algorithm discards them earlier), it accounts for the numerical dissipation as well. Since optimal geoemtries are shockless and non-dissipative, at the end the numerical dissipation would be the only contribution, which is an undesired effect. Finally, as previously stated, the last requirement is equivalent to maximize the throat area.

All these objectives have to be quantified into one or more functions to be minimized by the Genetic Algorithm. To select the number of objective functions it is necessary to examine the type of the desired characteristics. Excluding the total pressure, a three-objective optimization is nonetheless superfluous since the first two items can be combined together into a single objective representing the outflow quality. Moreover, a tradeoff exists between the nozzle length and such outflow quality because a reduction in the length clashes with outflow performance. So, a separated objective must be considered for the nozzle length, which makes the problem a two-objective.

While the second objective is of immediate formulation, the first objective requires a simple elaboration of the CFD output. On the outflow boundary the solution is a function only of the y coordinate and every variable of interest is known. Being $Z(y)$ the generic variable and Z_{trg} its target value

for the optimization, the mean absolute deviation weighed for the mass flow is computed as

$$\phi_Z = \frac{1}{\dot{m}} \int_0^{S_o} \rho(y)\mathbf{V}(y) \cdot \mathbf{n} \, |Z(y) - Z_{trg}| \, dy \tag{6.4}$$

where $\rho(y)$ is the densit and $\mathbf{V}(y) \cdot \mathbf{n}$ the component of the velocity normal to the boundary. With the finite-volume discretization, the domain boundary of interest is described by q cell boundaries, so that the integral 6.4 can be calculated as

$$\phi_Z = \frac{1}{\dot{m}} \sum_{j=1}^{q} \rho_j \mathbf{V}_j \cdot \chi_j \, |Z_j - Z_{trg}| \tag{6.5}$$

where the χ_j are metric vectors accounting for the orientation and the size of the generic j-th cell boundary (see [16] for their definition).

Computing in this way the functions related to the Mach number and flow angle, they can be combined to obtain the second objective function. To summarize, the multi-objective optimization problem statement reads

$$\min_{\mathbf{x}} f_1(\mathbf{x}) = \frac{1}{S_t} \tag{6.6}$$

$$\min_{\mathbf{x}} f_2(\mathbf{x}) = \frac{\phi_M}{\sigma_M} + \frac{\phi_\alpha}{\sigma_\alpha} \tag{6.7}$$

in which the σ_Z are user-defined weights and represent the deviation allowed from the target values, while the vector $\mathbf{x}$ contains the design variables.

6.3 Design Variables

From the type of parametrization employed has emerged the necessity to adopt at least the throat area S_t and the outflow dimesionless area s_o as design variables. The converging part is considered fixed in all its components because it is thought to have a minor influence on the outflow in the inviscid case. The present analysis assumes also the inflow section and the throat location fixed multiples of the throat section (reasonably $s_i = 1.75$ and $l_c = 3$), therefore the converging part is fixed in all its components. The throat curvature c_t also is a free variable.

As for the diverging part, the number of control points has to be selected. The approach is to fix their x_i coordinates, leaving only their vertical positions (controlled by the dimensionless η_i) as free variables. The figure 5.5 of the previous chapter shows that a cosine distribution throughout the diverging part better approximates the optimal geometry for a real gas, with only two control points. However, few conrol points seem to allow less flexibility in describing unconventional geometries. Such geometries have to be taken into account, especially when treating real gas cases.

Increasing the number of design variables slows down the optimization, but the quality of the solution benefits. For the present case, a cosine distribution with 3 control points is adopted, bringing the number of optimization variables to 6.

6.4 Constraints

Virtually, no additional constraint is necessary for this optimization. However, the search space is limited in the following:

- the throat section must generate $L_c < 1$, therefore $S_t < 1/l_c$;
- the outlet section must be greater than the throat section, therefore $s_o > 1$;
- the y_i of the control points must lay between the throat and the exit sections, therefore $0 < \eta_i < 1$.

Even the total pressure constraint is superfluous, because in general the shock-affected geometries do not generate a uniform outflow. However, during the selection the Genetic Algorithm tends to discard the individuals which violate the constraints, favoring the feasable designs. In this view, the following constraint on the mean outflow total pressure $P_{0,e}$ helps

$$\frac{P_{0,e}}{P_0} > 0.95 \tag{6.8}$$

In this view, if the total pressure difference between inflow and outflow is minimal, the flowfield is considered non-dissipative regardless of the actual loss given by the numerical dissipation or the weaker shocks.

6.5 Grid Generation

An elliptic grid generator allows to build the structured mesh which discretizes the domain, as shown in figure 6.1. The user-defined inputs are simply the number of nodes along the x and y directions. Increasing the number of nodes leads to an accurate solution of the flowfield, but is more expensive in terms of computational resources. With a Genetic Algorithm, tens or hundreds of simulations are foreseen to reach a good design, therefore an excessive mesh refinement would slow down the optimization too much. A compromise has to be reached between the accuracy of the results and the efficiency of the process.

For a nozzle running with ideal gas a reasonable choice is a grid of 150x40 nodes along the two directions [5]. A grid convergence study will be performed for the real gas nozzle in the following chapter, which confirms the present choice.

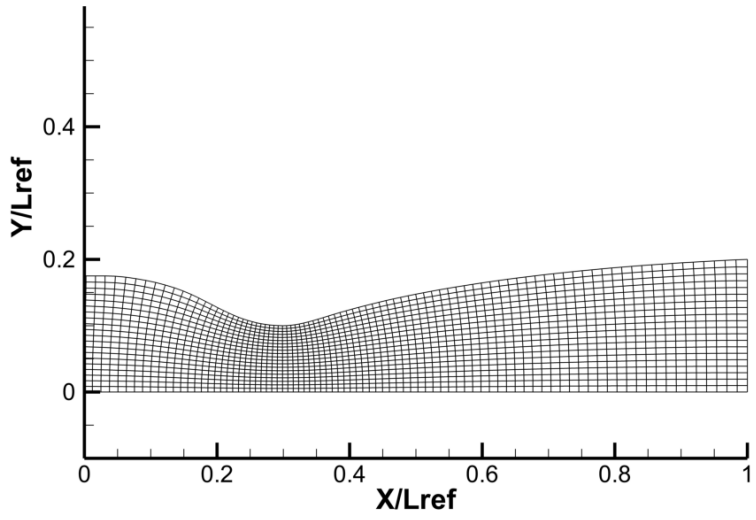

Figure 6.1: Example of a coarse structured mesh used for the ideal gas calculations

6.6 Metamodels

The metamodels represent a fundamental aspect to improve the efficiency of the optimization, being able to estimate the objective functions without recalling the time-consuming flow solver for every individual. Obviously, no metamodel is required for the throat preformance f_1 since it can be calculated directly from one of the inputs.

Firstly, whatever the model, it has to be trained. Two values of each designed variable are considered and the objective functions resulting from each combination are evaluated with zFlow. Each variable can take either a "low" or "high" value, positioned respectively at 25% and 75% of the design limits. Therefore, for the 6 variables of the problem under consideration, the initial training set is formed by $n_{train} = 2^6 = 64$ samples which should allow the metamodel to recognize the main trends of the input-output relations. Then, a test set is defined by selecting $n_{test} = 20$ random samples $\mathbf{x}_k$ from the design space and analyzing them with the flow solver. By comparing such results $f_2(\mathbf{x}_k)$ with the metamodel's prediction $\widetilde{f}_2(\mathbf{x}_k)$, the relative accuracy on the second objective is evaluated as

$$E = \frac{1}{n_{test}} \sum_{k=1}^{n_{test}} \frac{\left| \widetilde{f}_2(\mathbf{x}_k) - f_2(\mathbf{x}_k) \right|}{f_2(\mathbf{x}_k)} \tag{6.9}$$

The software modeFrontier has implemented a discrete variety of models, ranging from simpler polynomial approximations to more advanced models. Excluding from the analysis the simpler and more inaccurate methods together with those requiring a very large training set, the following are taken into consideration:

- Radial Basis Functions;
- Artificial Neural Networks;
- Kriging;
- Anisotropic Kriging;
- Gaussian Processes.

Setting the model's parameters to their default values, the test error is evaluated in figure 6.2 according to the equation (6.9). The initial predictions are very rough, but they should increase their accuracy throughout the optimization as the training database is expanded. From this analysis the Neural Networkis is clearly the worst-behaving model but, since it has already been employed in similar works [25], further investigations are undertaken.

Figure 6.2: Relative test error E_2 on the objective f_2 for different classes of metamodels

In particular for single-output metamodels, given the number of inputs $n_{in} = 6$ and the number of training samples $n_{train} = 64$, the maximum number of hidden nodes to have an overdetermined porblem for the calculation of the network parameters is

$$n_{hid} < n_{max} = \frac{n_{train}}{n_{in} + 2} = 8 \tag{6.10}$$

For the present case, the defalut settings use one hidden layer and 5 hidden neurons, but it has also been reported [1] that an underdetermined system (for example with $n_{hid} \approx 2n_{max}$) might perform better, inducing spourious oscillations which favour the exploration of a wider state space. The test error as function of the number of hidden nodes is reported in figure 6.3, and no clear trend emerges. Therefore, the Neural Networks are discarded in favour of the Kriging, which is also an exact predictor for the observed points (see section 4.3.3). Finally, remember that the optimization relies on the active learning of the metamodel throughout the process, to improve its predictive capability.

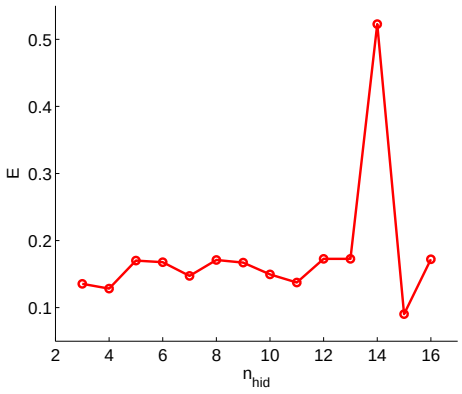

Figure 6.3: Relative test error E_2 on the objective f_2 for Neural Networks with varying hidden nodes n_{hid} and one hidden layer

6.7 Initial Population

Besides the surrogate models, some good individuals should be provided in the initial populaiton to further improve the efficiency of optimization. To do so, other easier perliminary optimizations (with less free variables and a single objective function) are built. Each of them fixes the throat section S_t, eliminating it from the design variables and fixing the nozzle length as well. Therefore the only objective considered is the outflow quality f_2. The control points are placed on the curve

$$\eta_i = 1 - (1 - \xi_i)^m \tag{6.11}$$

so that, being the abscissa fixed, the parameter m uniquely determines their coordinates (figure 6.4). Assuming also the throat curvaturee c_t as a fixed parameter, the only free variable left are the exponent m and the discharge section s_t. The resulting preliminary optimization is faster (involving fewer design variables), but constraints the control points on a pre-determined curve. For every throat section, the individuals with the better outflow quality are used to initialize the multi-objective optimization.

Figure 6.5 shows a result of the described procedure. The exponential constraint often leads to oblique shocks from the early stages of the diverging, nonetheless the discharge Mach number represents a good starting solution.

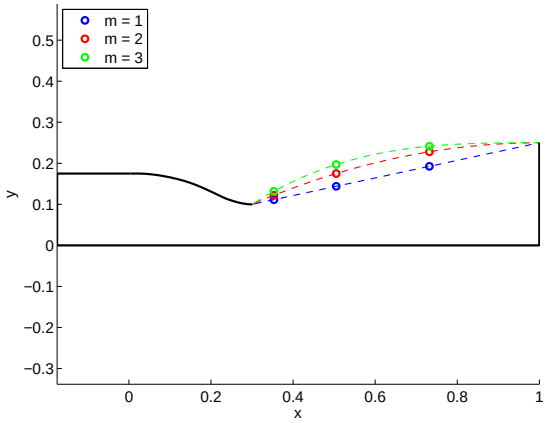

Figure 6.4: Position of the control points imposing the law 6.11, for different values of the exponent

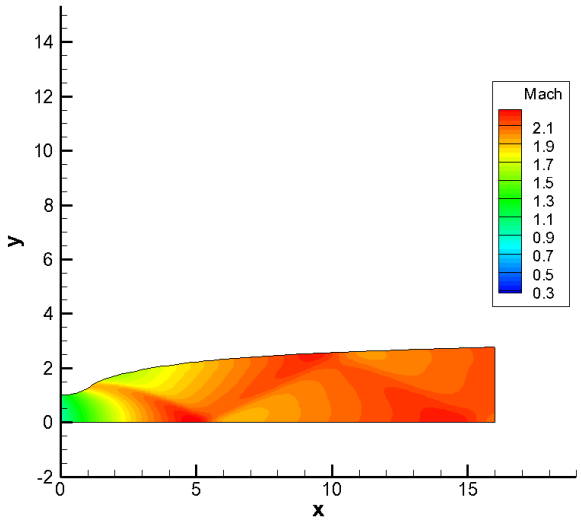

Figure 6.5: Example of a geometry obtained from the preliminary optimization

6.8 Results

For the present optimization the outflow quality is defined by the following tolerances:

- $\sigma_M = 0.025$;
- $\sigma_\alpha = 1^o$.

After the initial training of the surrogate model with 64 samples, a first optimization is run. Then, 5 individuals laying on the first pareto front are evaluated with the flow solver, allowing to extend the training database. The metamodel is re-trained and a more accurate optimization is performed. In this way, after few iterations, the first pareto front stabilizes and the optimization is considered concluded.

With the procedures just described, figure 6.6 shows the results of the Genetic Algorithm after the last training of the surrogate model. The four highlighted individuals are then analyzed with zFlow and the figures 6.7 and 6.8 report the results in term of outflow Mach number and flow angle, which determine the objective function f_2. Finally, figure 6.9 shows the diverging shapes of the nozzles and their lengths, to appreciate how shorter nozzles affect the quality of the solution. While the outflow angle always stays within the imposed tolerance of 1^o, the behavior of the Mach number is definitely not satisfactory for the shorter nozzles (cases C and D).

6.9 Concluding Remarks

The performed optimization concerns only the diverging part of the nozzle. The choice has been motivated by the limited influence the converging shape has on the outflow quality.

Comparing this methodology for nozzle design with the Method of Characteristics, the following differences emerge:

- the Method of Characteristics arbitrarily assumes the throat solution (which is not physical), while the present optimization arbitrarily assumes the converging shape (which can be physically imposed);
- the Method of Characteristics cannot treat subsonic flowfields, while the present optimization can, by simply adding to the design variables

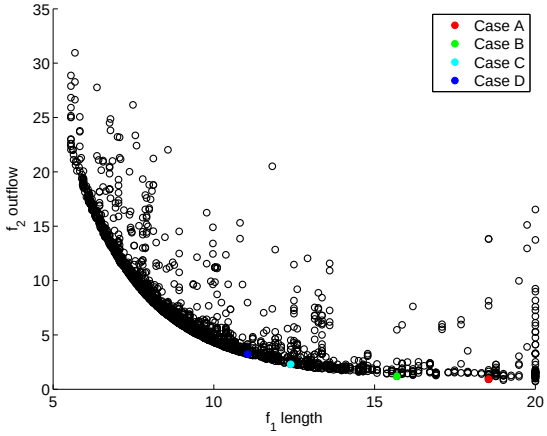

Figure 6.6: Results of the Genetic Algorithm after the last training. Individuals are evaluated with a Kriging model. The highlighted cases will be evaluated with the flow solver

some control points for the converging part and/or the location of the throat l_c;

- the Method of Characteristics cannot treat viscous or turbulent flowfields, while for the present optimization in principle it is possible (it depends whether the flow solver can);
- a multi-objective optimization with a Genetic Algorithm shows the tradeoff between different needs, allowing the designer a choice after the optimization is concluded.

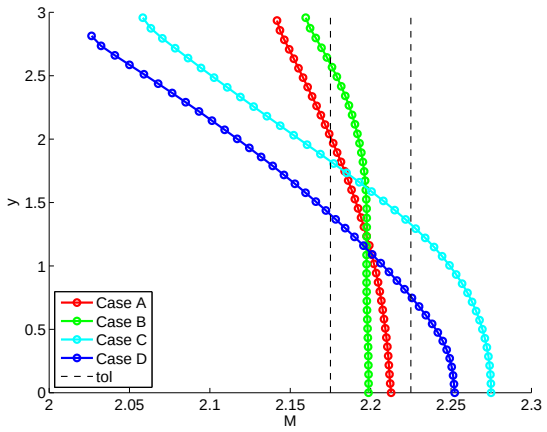

Figure 6.7: Mach number profile along the outflow section for the four selected cases

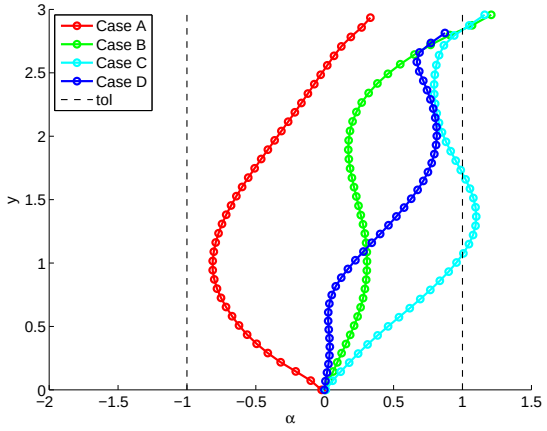

Figure 6.8: Flow angle profile along the outflow section for the four selected cases

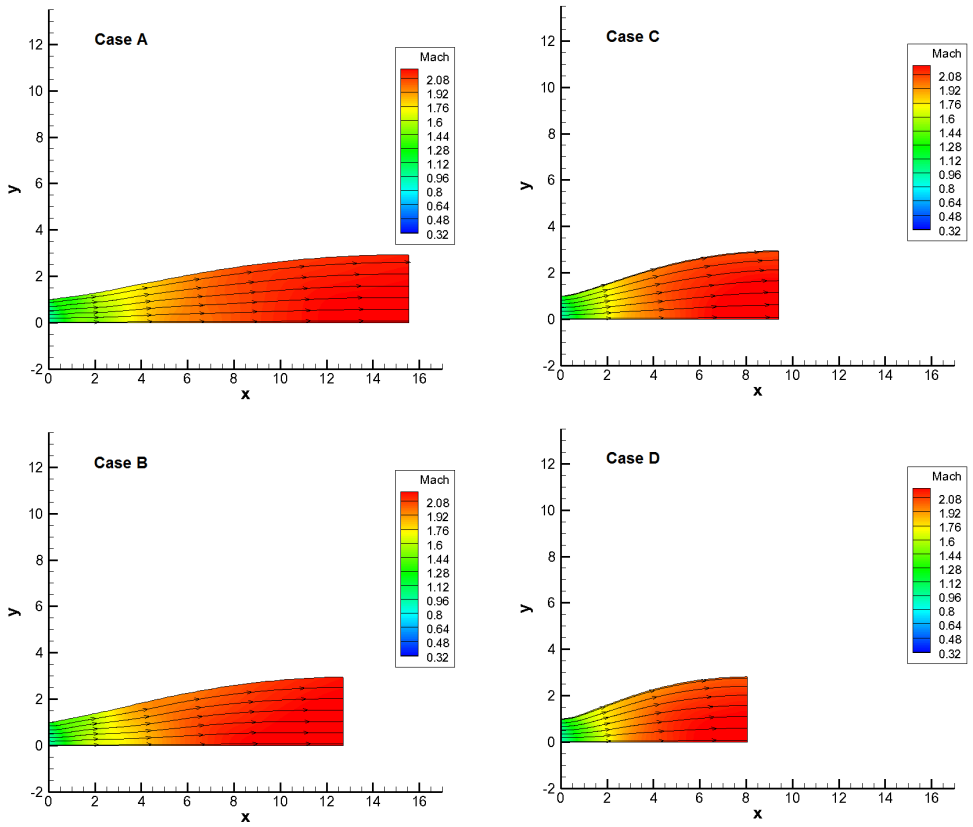

Figure 6.9: Diverging shapes of the nozzles for the four selected cases and Mach number distribution

Chapter 7

Optimization of a Real Gas Nozzle

– *What I do wrong?*
– *Ok, you did two things wrong.*

7.1 Introduction

In the previous chapter an optimization of a nozzle working with MDM was conducted employing an ideal-gas model. In the present chapter, the same type of optimization is carried out with a Span-Wagner equation of state. The considered expansion starts from supercritical reservoir conditions of $P_0 = 25\ bar$ and $T_0 = 310^o$C: as mentioned in section 2.2, supercritical cycle configurations have not been explored thoroughly yet, but might offer significant advantages. The goal remains a homogenious outflow Mach number of 2.2. The isentropic expansion, depicted in figure 7.1, passes very close to the saturation curve, therefore the real gas effects are expected to strongly influence the outcome.

In fact, an optimal shape according to the ideal gas model represents an unacceptable solution for this supercritical expansion. As an example, figure 7.2 shows that the real gas model predicts an outflow Mach number of 1.52, far below the target value.

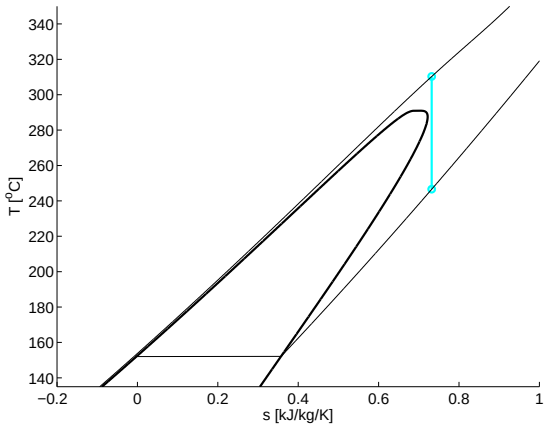

Figure 7.1: Supercritical expansion in the $T - s$ thermodynamic plane

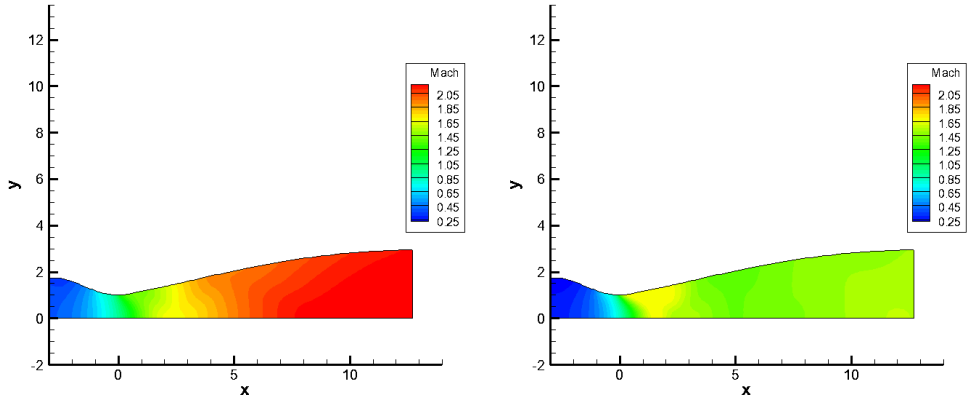

Figure 7.2: Optimal geometry for ideal gas. Comparison between ideal gas (left) and real gas (right) models

7.2 Grid Convergence Analysis

A grid convergence study is performed for the real gas on the nozzle of figure 5.4. That geometry is the result of a design with the Method of Characteristics for the same conditions ($P_0 = 25\ bar$, $T_0 = 310.3^oC$ and $M_e = 2.2$). The converging part is arbitrarily assumed, since it is not defined by the MoC.

Firstly, figures 7.4 report the results of an accurate simulation in terms of Mach number and pressure. Such distributions well reflect the results of the MoC (figure 5.4 [24]), giving a fairly uniform Mach number at the outflow section.

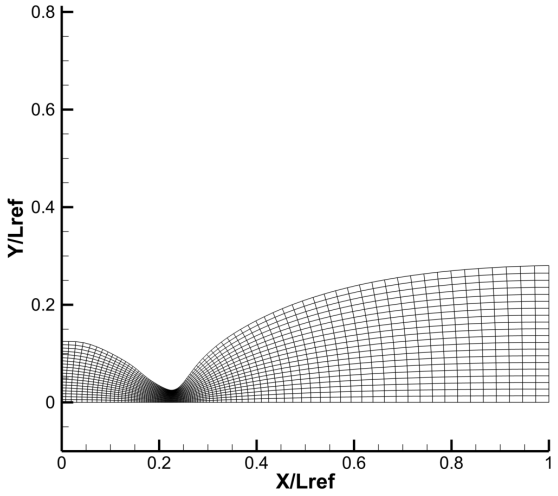

Figure 7.3: Example of a coarse structured grid used for the real gas calculations

The grid convergence study has been conducted as a function of the number of nodes either along the x and y coordinates. Two Mach numbers are taken as figures of merit at the outflow section: the first lays on the axis while the second is on the wall. Then the relative error is evaluated as

$$E = \frac{|M - M_{ex}|}{M_{ex}} \tag{7.1}$$

where as exact value M_{ex} is considered the result from the finest 400x80-node grid. From figure 7.5, also a relatively coarse grid of 100x20 nodes reduces

the error to 1%. However, for all the inviscid optimizations, a grid of 150x40 nodes has been employed, which makes the solution almost grid-independent, confirming also the choice for the ideal gas grid.

7.3 One Dimensional Analysis

Similarly to the previous chapter, to have a preliminary idea of the dimensions of the nozzle, a one-dimenisonal isentropic approach is followed. The thermodynamic properties of MDM, as results of the Span-Wagner equation of state, are calculated with FluidProp [18].

With a real gas model there is no direct relation such as equation 6.3 to estimate the throat-to-exit area ratio and some intermediate passage is needed. So, the entropy of the fluid is firstly calculated from the known reservoir conditions P_0 and T_0 as

$$\widetilde{s} = s(P_0, T_0) \tag{7.2}$$

Then, according to the energy conservation is

$$h(P_0, \widetilde{s}) = h(P, \widetilde{s}) + M\frac{c^2(P, \widetilde{s})}{2} \tag{7.3}$$

Since the flow is considered isentropic, equation 7.3 determines the pressure P corresponding to a given Mach number M. In case of supersonic outflow the nozzle is chocked, therefore imposing $M_t = 1$ in equation (7.3) determines the throat pressure P_t. Then, imposing $M_e = 2.2$ for the outflow determines the discharge pressure P_e. At this point every thermodynamic variable is known at the throat and at the outflow as function of (P, s). The mass conservation law allows to calculate the area ratio as

$$\frac{S_e}{S_t} = \frac{\rho_t c_t}{\rho_e M_e c_e} = 10.537 \tag{7.4}$$

This area ratio is three times that of the ideal gas model.

7.4 Results

Keeping the same converging geometry of the ideal gas case, the diverging shape is here optimized. Again, an initial training database for the metamodel is made of 64 samples and it is successively refined. The optimization

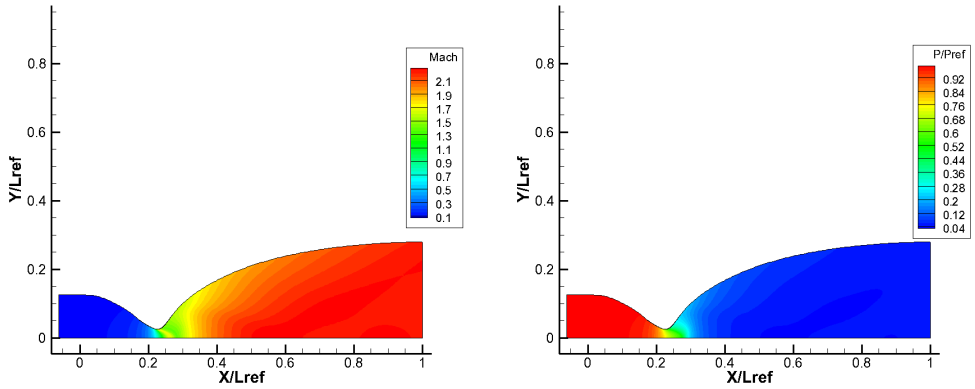

Figure 7.4: Mach number (left) and pressure (right) distributions for the test case of MDM at reservoir conditions of $P_0 = 25$ bar and $T_0 = 310^o$C

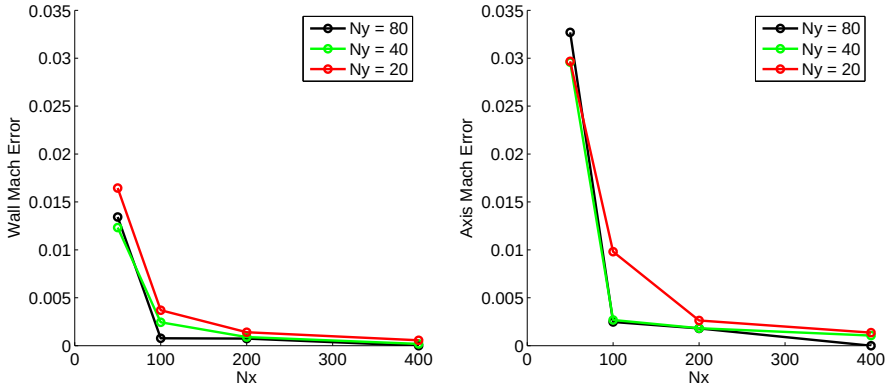

Figure 7.5: Relative error on the outflow Mach number at the wall (top) and at the axis (bottom)

is stopped when the first pareto front stabilizes and re-trainings do not bring actual improvements anymore. The present optimization has been stopped after 150 direct zFlow evaluation, which means that about 90 re-training samples have been used. This is found to be sufficient, since the test set employed to verify the accuracy of the metamodel shows limited improvements in the later stages of the re-training (figure 7.6).

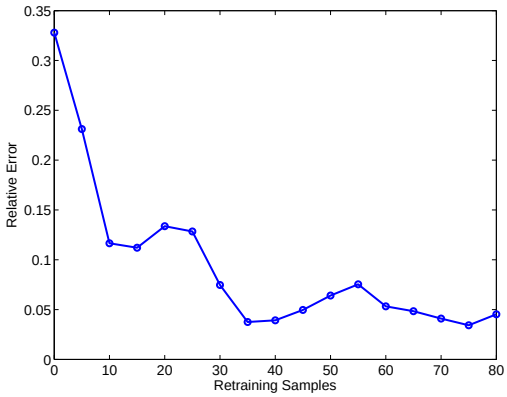

Figure 7.6: Relative error of the metamodel as function of the additional re-training samples. The test set is made of 10 samples

After the last training of the surrogate model, figure 7.7 shows the results of the evolution according to the Kriging model. Again, four individuals laying on the first pareto are selected and analyzed with zFlow and the figures 7.8 and 7.9 show the results in term of outflow Mach number and flow angle. Finally, figure 7.10 shows the diverging shapes of the nozzles and their lengths. For the longer nozzles (cases A and B) the Mach number never exceeds the imposed tolerance, while for the shorter the outflow uniformity is not well attained.

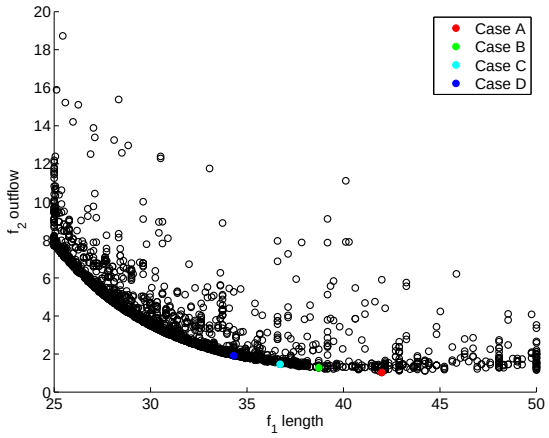

Figure 7.7: Results of the Genetic Algorithm after the last training. Individuals are evaluated with a Kriging model. The highlighted cases will be evaluated with the flow solver

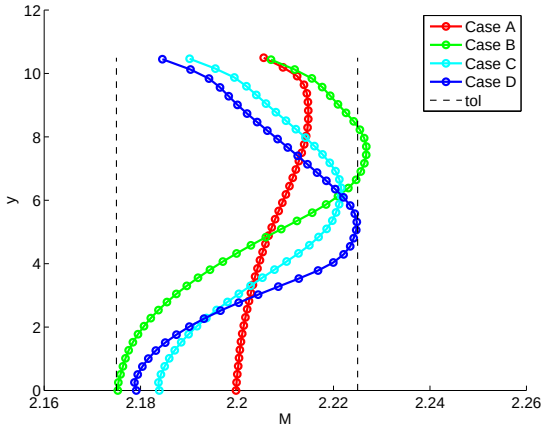

Figure 7.8: Mach number profile along the outflow section for the four selected cases

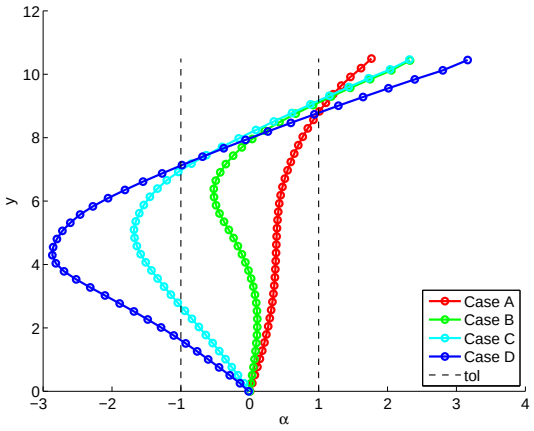

Figure 7.9: Flow angle profile along the outflow section for the four selected cases

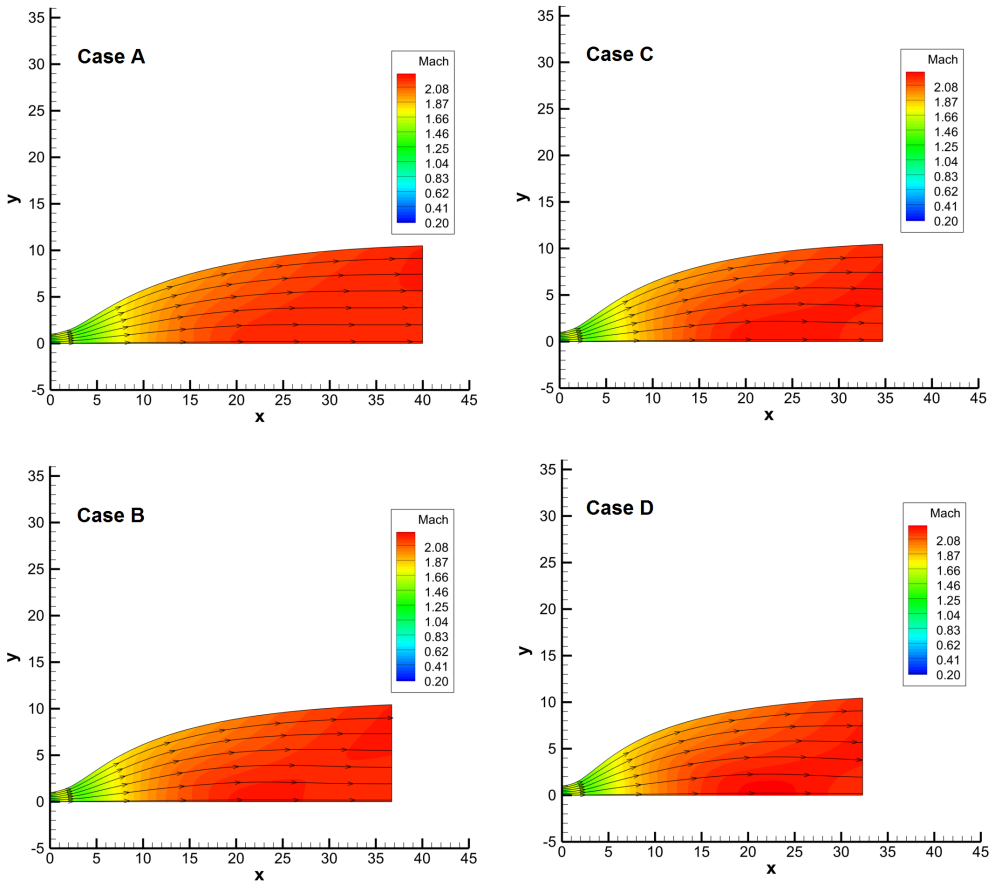

Figure 7.10: Diverging shapes of the nozzles for the four selected cases and Mach number distribution

7.5 Comparison with the Ideal Gas

The same optimization leads to very different results depending on which gas model is employed, see figure 7.2. An optimum real gas nozzle is 3 times bigger than its ideal gas counterpart, thus real gas effects cannot be neglected in proximity of the critical point.

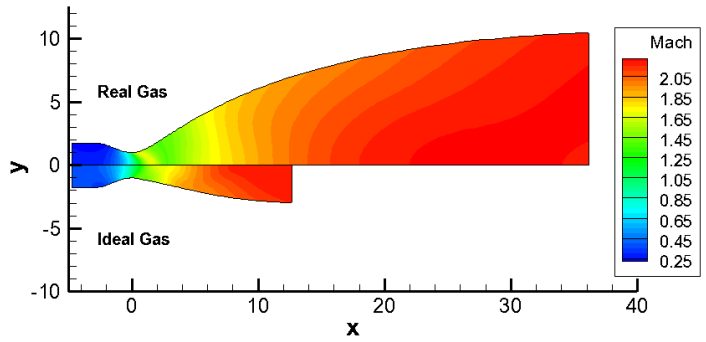

Figure 7.11: Comparison of two optimal geometries according to ideal and real gas models

Such differences can be explained by looking at some thermodynamic quantities. Figures 7.12 and 7.13 show the speed of sound and the fundamental derivative as functions of the pressure along the isentropic expansion. Depending on the gas model employed, the throat conditions vary, with the throat pressure predicted by the real gas being slightly higher[1]. According to the real gas model the speed of sound is almost constant during the expansion, so that an increase in the velocity leads immediately to an increase in the Mach number. However, the real gas predicts an increasing speed of sound along most of the diverging part, so that the Mach number growth is slower. Such trend of the speed of sound has been well documented also for a van der Waals model [12], with a minimum close to the critical point.

Moreover, by recalling the quasi one-dimensional flow relation [4]

$$\frac{dM}{dx} = \frac{1 + (\Gamma - 1)M^2}{M^2 - 1} \frac{M}{S} \frac{dS}{dx} \tag{7.5}$$

[1] On the right of those conditions, at lower pressures, the flow is supersonic

with S the local nozzle section, it is clear that the lower is Γ, the slower is the increase in the Mach number for the same geometry variation.

So, in the early stages of the diverging the real gas predicts both a higher Γ and more rapid Mach number growth (see figures 7.13 and 7.2). Then the fundamental derivative decreases and this effect leads necessarily to a longer nozzle with a bigger outflow section.

7.6 Influence of the Converging Part

To asses the influence of the converging part on the outflow, further investigations are undertaken. Always referring to the inviscid case, the three geometries of figure 7.14 are analyzed. They have the same diverging part, resulting from the optimization, while the converging is given arbitrarily.

Figure 7.15 reports the three Mach number profiles at the outflow. The Mach number varies very little in comparison to the refernece tolerance, so that considering a fixed converging in the optimization is reasonable. The Method of Characteristics designs only the diverging part, but it assumes the throat flowfield. This solution, though it is theroetically based, presents the problem of finding a converging part which would lead to such flowfield.

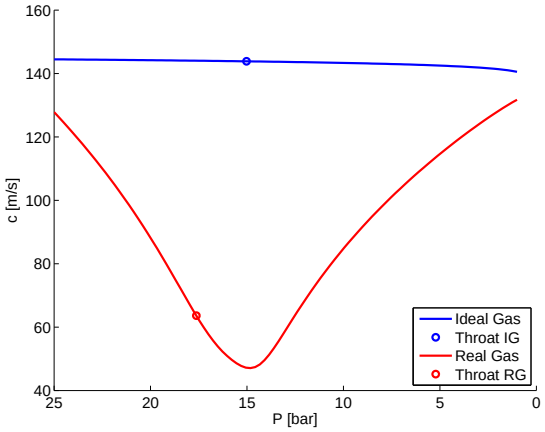

Figure 7.12: Speed of sound $c = c(P, \tilde{s})$ as function of the pressure along the isentropic expansion. The expansion starts at $P_0 = 25\ bar$, $T_0 = 310^o C$

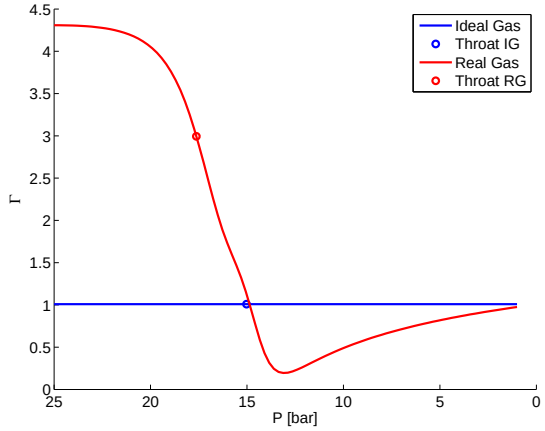

Figure 7.13: Fundamental derivative $\Gamma = \Gamma(P, \tilde{s})$ as function of the pressure along the isentropic expansion. The expansion starts at $P_0 = 25\ bar$, $T_0 = 310^o C$

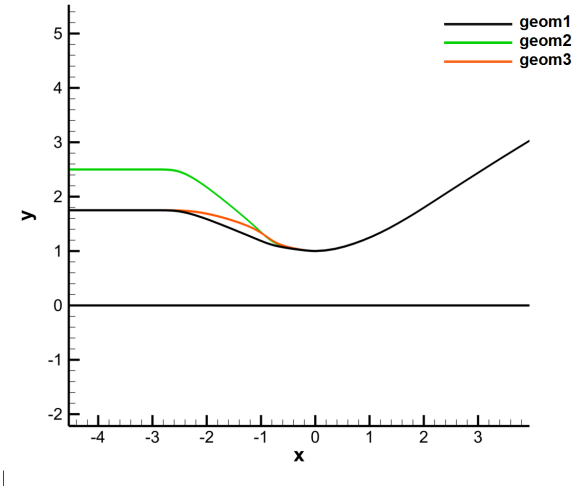

Figure 7.14: Geometries tested to evaluate the invluence of the converging part on the outflow

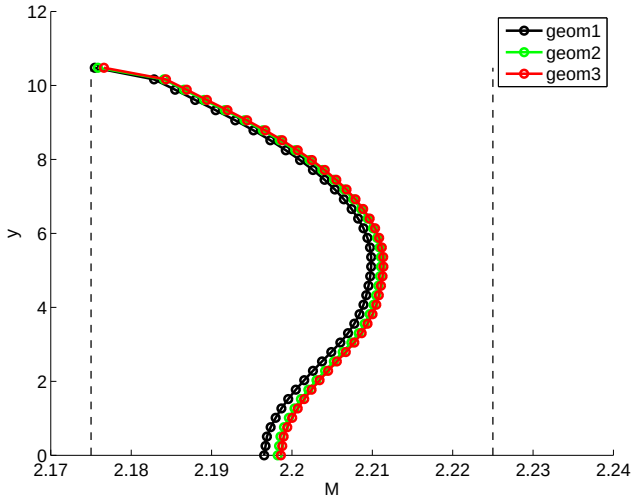

Figure 7.15: Outflow Mach number for the three converging geometrie tested

Chapter 8

Optimization in Subcritical Conditions

– Yeah, he does like to repeat himself.

8.1 Introduction

The previous chapter showed a significant difference in the shape of the optimal nozzle for a supercritical expansion depending on the thermodynamic model adopted to describe the gas. The present chapter aims at the optimization of a nozzle from subcritical reservoir conditions. In particular, $P_0 = 10$ bar and $T_0 = 276.9^oC$ are chosen, while the outflow Mach number is still 2.2, to be able to compare the results with the previous calculations. Such expansion is represented in the $T - s$ thermodynamic plane in figure 8.1.

The behavior of the speed of sound and of the fundamental derivative is shown in figures 8.2 and 8.3. Differently from the supercritical expansion, they now exibit monotonic trends, both tending to the ideal gas behavior for low pressures. For these reasons, the nozzle shape should be closer to the ideal gas prediction.

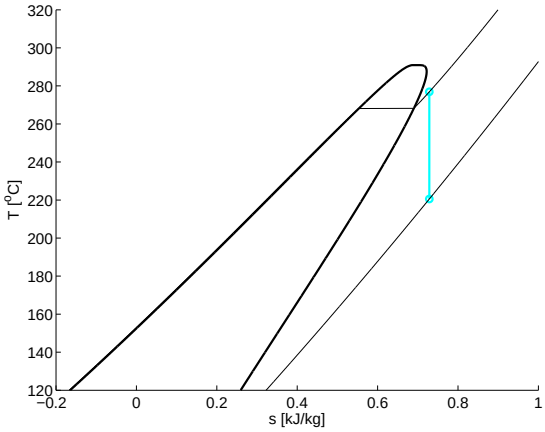

Figure 8.1: Subcritical expansion in the $T - s$ thermodynamic plane

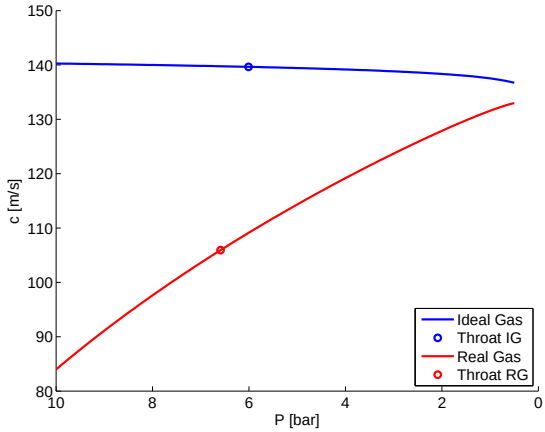

Figure 8.2: Speed of sound $c = c(P, \tilde{s})$ as function of the pressure along the isentropic expansion. The expansion starts at $P_0 = 10\ bar$, $T_0 = 276.9^o C$

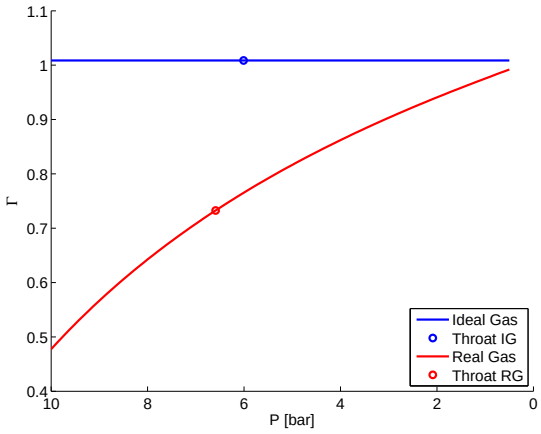

Figure 8.3: Fundamental derivative $\Gamma = \Gamma(P, \tilde{s})$ as function of the pressure along the isentropic expansion. The expansion starts at $P_0 = 10\ bar$, $T_0 = 276.9^oC$

8.2 Results

The results of the optimization are shown in figure 8.4 according to the Kriging model. As always, four individuals are taken and evaluated with the flow solver. The outflow is reported in figure 8.5 and 8.6. Finally, the shapes of the four nozzles are in figure 8.7.

8.3 Recap

The subcritical optimization has brought a lenght of the diverging part comparable to the ideal gas results, even though with a bigger outflow section. Furthermore, while in the supercritical expansion the Mach number is non-monotonic along x, in the subcritical expansion such oscillatory behavior is much less pronounced. As mentioned, this is due to the fundamental derivative which assumes higher values in the subcritical case.

Table 8.1 summarizes the results for the inviscid cases. No total condition is needed for the ideal gas case because the pressure and area ratios are ruled only by the specific heat ratio γ. Therefore, the ideal gas column might also represent an expansion occurring in a dilute gas region, for which the ideal

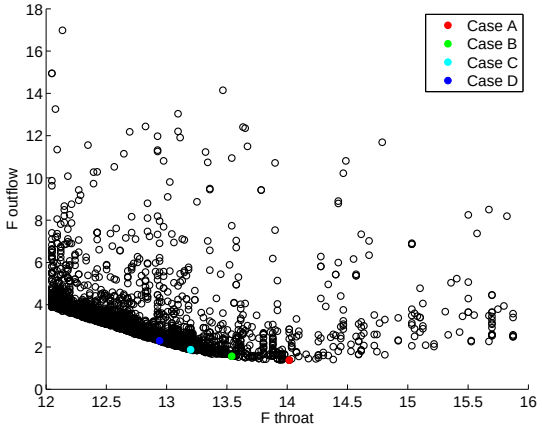

Figure 8.4: Results of the Genetic Algorithm after the last training. Individuals are evaluated with a Kriging model. The highlighted cases will be evaluated with the flow solver

gas law is valid. In this view, moving towards the saturation curve alters first of all the discharge pressure ratios, with the ideal gas model prediction being twice bigger than the supercritical case. The compressibility factor $Z = Pv/RT$ strongly reduces towards the critical point, confirming the assertion made in chapter 2 about the lower specific volumes for the same pressure and temperature. The throat-to-exit area ratios are calculated with the one-dimensional isentropic relations, while the diverging lengths l_d are the results of the optimizations. They are made nondimentional with the throat section, namely $l_d = (1 - L_c)/S_t$ from figure 5.1.

Then, rescaling the ideal gas results to the total conditions of the subcritical and supercritical expansions, the mass flow can be calculated in the two cases

$$\frac{\dot{m}}{S_t} = \rho_t u_t \tag{8.1}$$

with respect to the throat. Table 8.2 shows again a big difference for the supercritical expansion, in which the mass flow doubles from the ideal to the real gas model. A difference of 8% concerns the subcritical case, despite consistent variations affect both the sonic density and velocity, but they partly compensate.

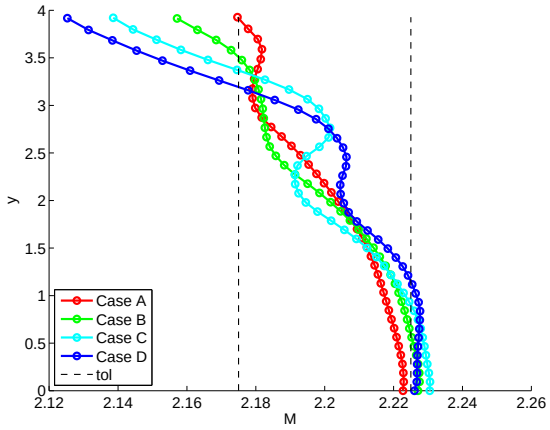

Figure 8.5: Mach number profile along the outflow section for the four selected cases

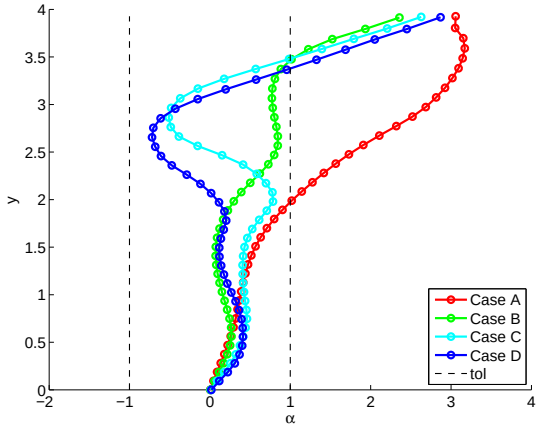

Figure 8.6: Flow angle profile along the outflow section for the four selected cases

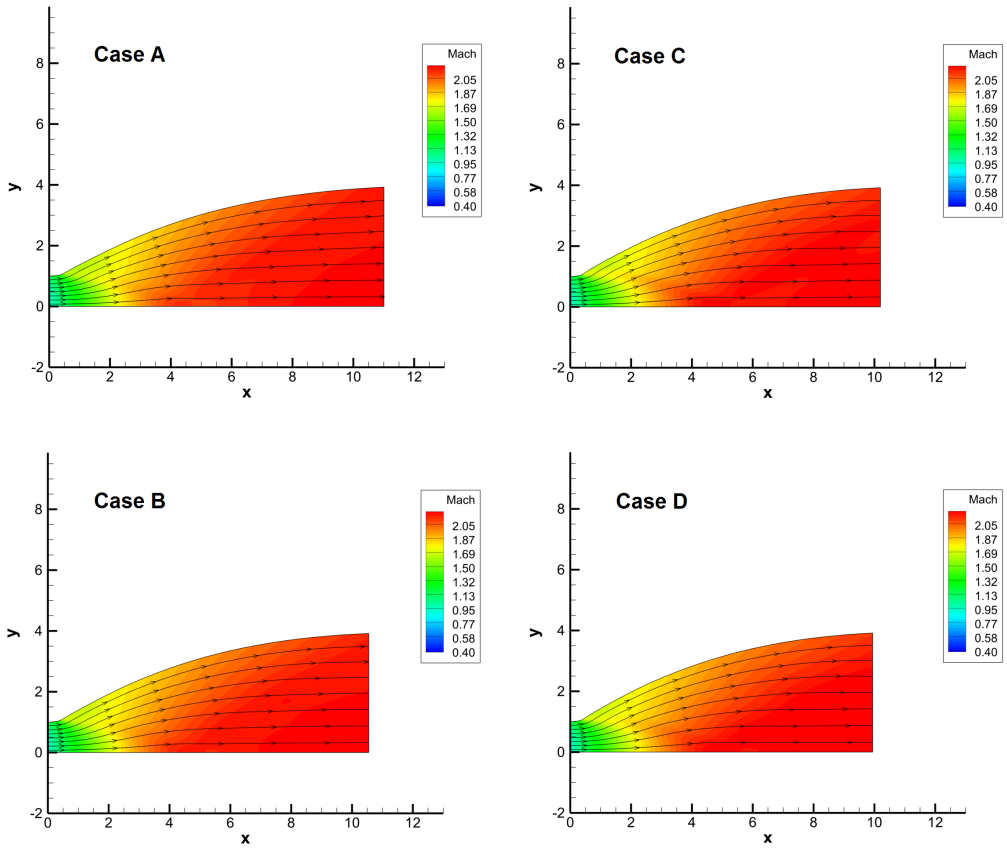

Figure 8.7: Diverging shapes of the nozzles for the four selected cases and Mach number distribution

Table 8.1: Summary of the conditions analyzed for the inviscid optimizations

	Dilute Gas	Subcritical	Supercritical
Total Temperature T_0 $[^oC]$	–	276.9	310.3
Total Pressure P_0 $[bar]$	–	10	25
Throat Pressure Ratio P_t/P_0	0.603	0.659	0.705
Outflow Pressure Ratio P_e/P_0	0.090	0.074	0.046
Reservoir Complessibility Factor Z_0	1.000	0.623	0.306
Throat Complessibility Factor Z_t	1.000	0.766	0.278
Outflow Complessibility Factor Z_e	1.000	0.973	0.959
Outflow Area Ratio S_e/S_t	3.008	3.933	10.537
Typical Diverging Lenght l_d	12	11	35

Table 8.2: Mass flow, comparison between ideal and real gas models

	ρ_t $[kg/m^3]$	u_t $[m/s]$	$\dot{m}/S_t$ $[kg/m/s]$
Subcritical			
Ideal Gas	31.4	139.6	4390
Real Gas	45.2	105.9	4787
Supercritical			
Ideal Gas	74.1	143.8	10657
Real Gas	313.0	63.6	19919

Chapter 9

Geometry Optimization Accounting for Viscous Effects

– What you learn tonight?

9.1 Introduction

The present task is to perform the same shape optimization as chapter 7 accounting for the viscous effects. The software zFlow is able to solve both the laminar and the Reynolds-averaged compressible Navier-Stokes. However, the turbulent version of the software has not displayed acceptable robustness, therefore this section is limited to the laminar effects only.

Anyway, the Reynolds number comes into play and it is calculated from:

- L_{ref} which is the nozzle total length, resembling the chord of a blade;
- V_{ref} given by the outflow Mach number and sound speed;
- ρ_{ref} and μ_{ref} given by the outflow conditions as well.

Accurate transport properties are not available in zFlow for the MDM, so they are calculated with simpler models. For example the viscosity is a function of the temperature by the following power-law:

$$\mu = \mu_{ref} \left(\frac{T}{T_{ref}} \right)^{\alpha} \tag{9.1}$$

which indeed is a strong approximation. Figure 9.1 shows the difference in the viscosity along the isentropic expansion considered in the previous analysis. In the present cases, $\alpha = 1.5$ is considered the most appropriate to obtain a good approximation in the last phases of the expansion.

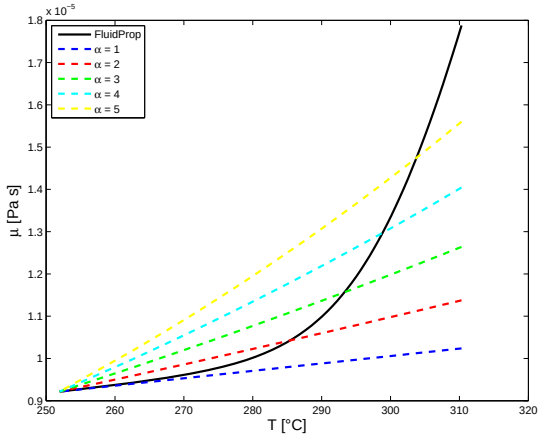

Figure 9.1: Viscosity $\mu = \mu(T, \tilde{s})$ along the isentropic expansion from $P_0 = 25$ *bar* and $T_0 = 310^o C$ to the design Mach number $M = 2.2$. Comparison between the accurate estimation from FluidProp and the power-law 9.1

9.2 Validation of the Flow Solver over a Flat Plate

Before starting the optimization of the nozzle, the flow solver is validated over a flat plate at zero angle of incidence. The validation case concerns air (treated as ideal gas) in the laminar regime. The simulations are performed at $M = 0.3$ to resemble an incompressible flow, and $Re = 6.75 \cdot 10^6$ based on the length of the plate ($L = 1\ m$). The origin of the reference frame is located on the leading edge of the plate, while the computational domain allows for a uniform inflow and extends to the end of the plate. The grid adopted is shown in figure 9.2 and it is refined in proximity of the wall (the first cell has a dimensionless height of $2.78 \cdot 10^{-6}$ based on the plate length).

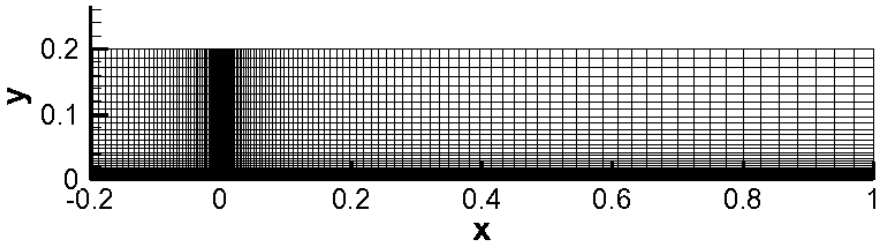

Figure 9.2: Flat plate computational grid

The laminar case is compared to the Blasius exact solution. Firstly, the velocity at the outflow is compared in figure 9.3, plotting the two nondimensional components with respect to the similarity variable η

$$\eta = \sqrt{\frac{U_\infty}{\nu_\infty x}} y \tag{9.2}$$

where U_∞ is the asintoptic velocity and ν_∞ is the kinematic viscosity. Secondly, since Blasius theory gives also the friction coefficient distribution along the plate as

$$C_f = \frac{0.664}{\sqrt{Re_x}} \tag{9.3}$$

this comparison is made in figure 9.4. As for the laminar case, the zFlow results are in good agreement with the theory.

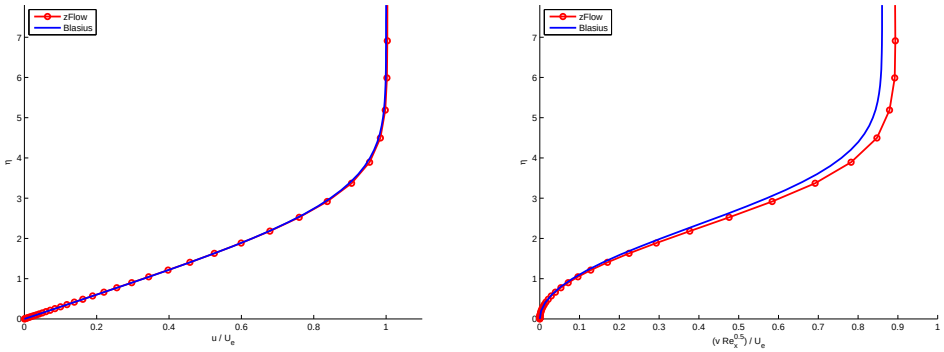

Figure 9.3: Velocity profiles for the laminar flat plate

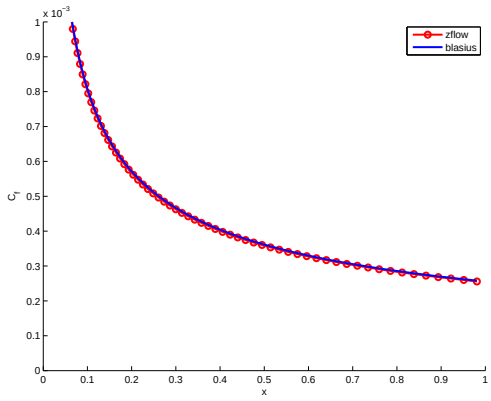

Figure 9.4: Friction coefficient along the flat plate, laminar case

9.3 Problem Definition

As shown in chapter 5, the absence of a reference length in the Euler equations made every rescaling possible without any consequence. In that case, the problem could be formulated equivalently as a maximization of the throat area with fixed length, or as a minimization of the total length with fixed throat. For the viscous problem, the choice of a reference length makes this assertion false, allowing two distinct formulations of the optimization problem:

1. **Fixed Throat, Variable Length**

   In the first approach the throat section is imposed, while the total length of the nozzle varies, thus varying the Reynolds number. The present formulation consists of minimizing the total length while maximizing the outflow quality. Since the throat section rules the mass flow, this is the better approach for the TROVA facility in which the high pressure reservoir has been designed to guarantee certain running times.

2. **Fixed Length, Variable Throat**

   A second approach consists of fixing the total lenght of the nozzle and the Reynolds number. This formulation aims at maximizing the throat

section and seems better for turbine blades, in which the mass flow can be adjusted by changing the number of nozzles for the stage.

Therefore, the throat height is fixed to $h_t = 11\ mm$, which is acceptable in terms of running times and leads to neglectable blockage effects when inserting the pressure probes [9]. Sticking with the same parametrization as figure 5.2, the reference length is given by

$$L_{ref} = \frac{h_t}{S_t} \tag{9.4}$$

9.4 Design Variables and Objectives

Nine variables are accounted for the viscous optimization:

- one control point for the converging part;
- five control points for the diverging part;
- the parameter S_t, which essentially determines the nozzle length;
- the throat curvature c_t;
- the outflow section s_o.

A two-objective problem is still the the best choice, with one function related to the length and the other to the outflow. However, the outflow objective accounts also for dissipation in terms of total pressure losses, because they are maily due to viscosity, with the numerical dissipation becoming neglectable. Therefore, the multi-objective optimization problem statement reads

$$\min_{\mathbf{x}} f_1(\mathbf{x}) = \frac{1}{S_t} \tag{9.5}$$

$$\min_{\mathbf{x}} f_2(\mathbf{x}) = \frac{\phi_M}{\sigma_M} + \frac{\phi_\alpha}{\sigma_\alpha} + \frac{\phi_P}{\sigma_P} \tag{9.6}$$

in which the ϕ_Z represent the mean error to the target, and the σ_Z are user-defined weights (see section 6.2). The target values and tolerances are reported in table 9.1.

No constraint is imposed because the total pressure is now part of the objectives.

Table 9.1: Target values and tolerances for the viscous optimization

Z	Z_{trg}	σ_Z
M	2.2	0.025
α [deg]	0.0	1.0
$P_{0,e}/P_0$	1.0	0.1

9.5 Mesh Generation

The domain simulated for the viscous calculations is shown in figure 9.5. A straight path is added before the nozzle, so that the inflow condition of uniform flow is still valid. Therefore the boundary layer starts to develop from an infinitely sharp leading edge representative of the beginning of the nozzle.

Then, the mesh has to be refined in proximity of the wall: the height h_1 for the first computational cell should give $y^+ \approx 1$. By the definitions of the nondimensional wall distance and the friction velocity

$$y^+ = \frac{h_1 u_\tau}{\nu} \tag{9.7}$$

$$u_\tau = \sqrt{\frac{\tau_w}{\rho}} \tag{9.8}$$

it is clear that finding h_1 requires an estimation for the shear stress at the wall τ_w, or the friction coefficient. Such estimation is made according to equation 9.3, valid for the flat plate.

The number of nodes along the y direction is selected to achieve the same mesh resolution far from the wall as in the inviscid case (figure 9.6).

9.6 Results

The procedure is the same as in the previous chapters: a database is initially created and successively refined to train the metamodel. The optimization is run with the surrogate and after the last retraining, figure 9.7 is obtained. Again, some cases are selected and analyzed with the flow solver to show

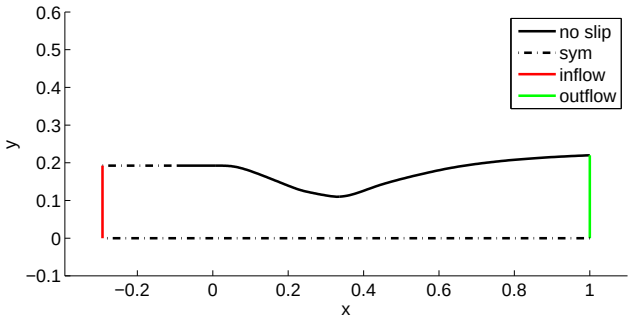

Figure 9.5: Domain and boundary conditions for the viscous simulations

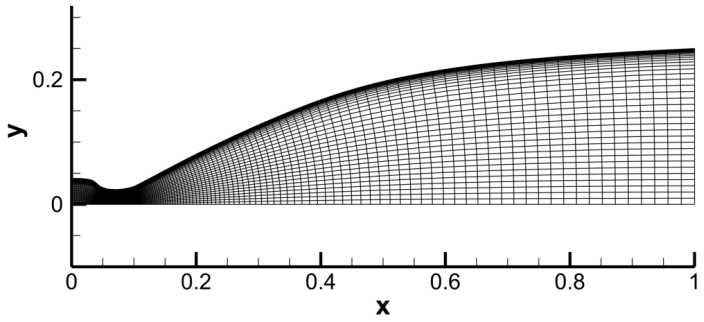

Figure 9.6: Mesh for the viscous calculations

how a reduction in the length affects the outflow. Figures 9.8 and 9.9 show the results in term of Mach number and outflow angle.

Firstly, by looking at the outflow angle profile a longer nozzle seems necessary according to the laminar solution with respect to their inviscid counterparts. However, the bigger contribution to the outflow objective function comes still from the Mach number. This is due mainly to the boundary layer, where the velocity decreases and where the target Mach number cannot be reached. The shape of the nozzles is reported in figure 9.10.

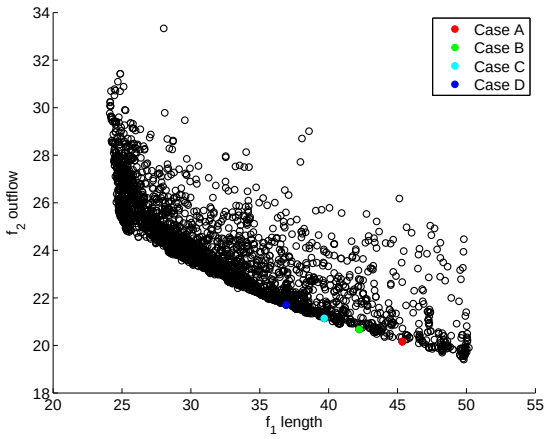

Figure 9.7: Results of the Genetic Algorithm after the last training. Individuals are evaluated with a Kriging model. The highlighted cases will be evaluated with the flow solver

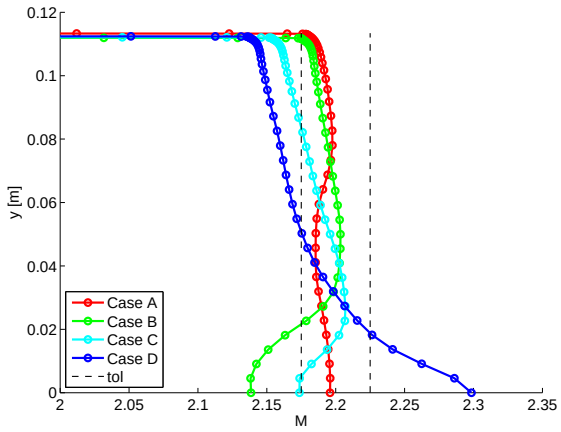

Figure 9.8: Mach number profile along the outflow section for the four selected cases

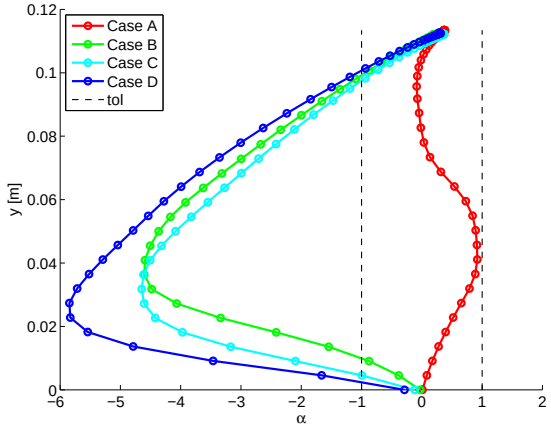

Figure 9.9: Flow angle profile along the outflow section for the four selected cases

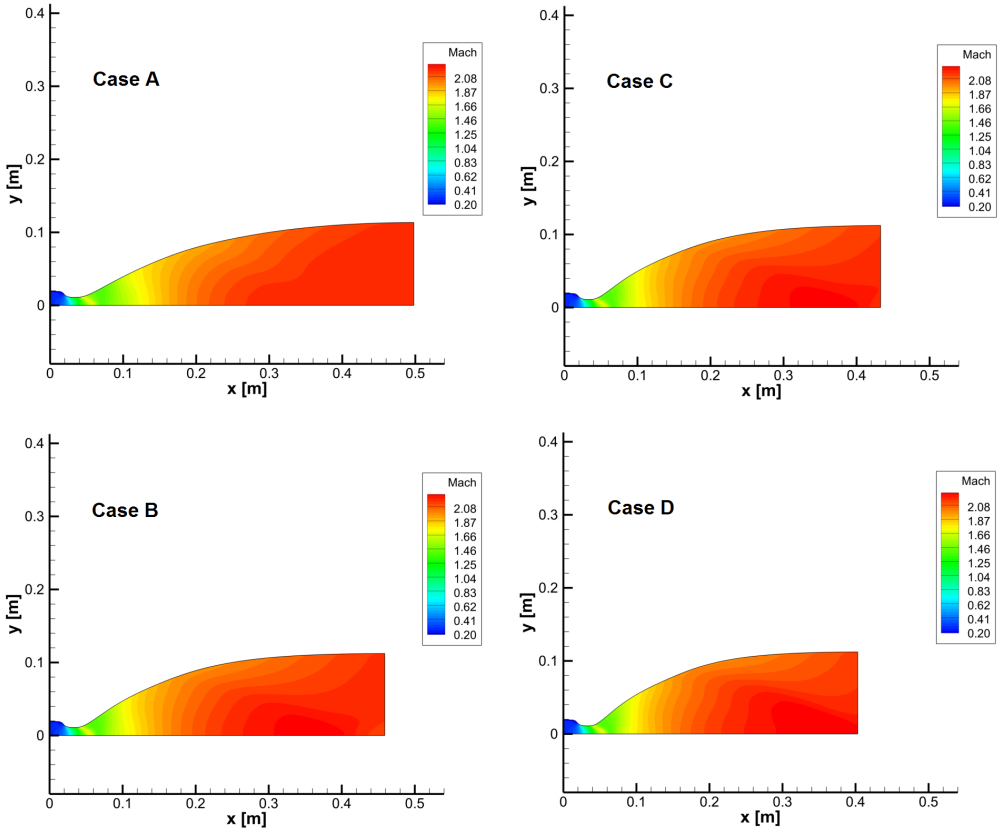

Figure 9.10: Diverging shapes of the nozzles for the four selected cases and Mach number distribution

Chapter 10

Conclusions and Perspectives

– Maybe someone oughta count to ten.

10.1 Conclusions

The total conversion efficiency of energy conversion systems is dependent on the efficiency of its components. This thesis tests a methodology for the fluid dynamic design of turbomachinery components for Organic Rankine Cycles in order to improve their overall efficiency. The methodology employs a Genetic Algorithm (GA) coupled with the CFD solver to optimize the shape of a converging-diverging two dimensional nozzle operating in the dense gas regime. This nozzle could be used in the *Test Rig for Organic Vapor* wind tunnel to perform experiments on organic fluids.

Usually, the Organic Rankine Cycles operate with heavy compounds in the thermodynamic region close to the critical point. In such conditions, neglecting the real gas effects leads to design not fulfilling the expectations. For example, the present work highlights how the ideal gas approach underestimates the size of the nozzle by three times in a supercritical expansion. This is due to the non-ideal and non-monotonic behavior of the speed of sound, which is seen to increase during a large part of the expansion. Accounting for the viscous effects does not alter such conclusions.

In principle, GAs allow for automatic optimizations if every component which they interact with (for example geometry modeler, mesh generator, CFD analysis and post processor) can work without external intervention.

In this view, robustness is the most pressing issue to reach for the flow solver, which should be able to converge to the solution for any geometry the GA asks for. zFlow displayed an excellent level of reliability for both the inviscid and the viscous cases. The importance of using in-house non-commercial softwares for both the flow solution and the estimation of the thermophysical properties of the gas lies in the knowledge of how the calculations are performed and their level of accuracy. Moreover, if the solver crashes somewhere in the analysis, it can be improved to overcome such problems, while with a commercial software that is not possible.

On the other hand, the GA-based approach is very expensive from a computational standpoint, because numerous CFD analysis are required to reach a satisfactory design. However, improvements on the time efficiency of the process are possible by employing different levels of sophistication for the flow analysis, or even replacing it with a surrogate model. Such models are trained to reproduce the input-output relation (namely they can estimate the performance of a nozzle for a given geometry) and their prediction accuracy can be refined during the course of the optimization. While the quality of the results remain very good, the number of the flow analysis is reduced by 90%, thus resulting in a consistent save of time.

10.2 Perspectives

The future for the Organic Rankine Cycles seems very bright, but the knowledge on organic fluids can still be improved, especially in the supercritical conditions. Accurate thermodynamic properties are available only for a limited set of fluids and new experimental data are necessary to characterize a wider set of substances.

Similarly, the TROVA wind tunnel initially aims at the calibration of pressure probes in a converging-diverging nozzle for different organic fluids in those particular conditions. Successively, tests on blade cascades are foreseen, which would ultimately lead to direct measurments in industrial turbines.

On the other hand, the GA-based optimization is a very promising technique for turbomachinery design, especially with the growing computational power available nowadays. By the way, when facing complex geometries and complex equations of state for the description of the fluid, it is the only viable way. Its limitations are basically set by the other softwares recalled,

namely the mesh generator and the flow solver. While the results of this work have been carried out with a structured grid generator appropriate for simple geometries, other tools have been developed [26] to obtain automatically a mesh in high-Reynolds regimes for arbitrary complex geometries.

The CFD solver zFlow is a powerful tool to simulate real gas flows. Currently it displays a questionable robustness for the turbulent calculations which does not allow a reliable coupling with the optimizer. However, it is still under development for various aspects and the project's conclusion is scheduled within a few years.

Bibliography

[1] J. Harinck. *Super- and Transcritical fluid expansions for next generation energy systems*. PhD thesis, Technische Universiteit Delft, Delft, 2010.

[2] M. Gaia G. Angelino and E. Macchi. A review of italian activity in the field of organic rankine cycles. In *Proceedings of the Intl.VDI Seminar (Verein Deutsche Ingenieure)*, VDI-Dusseldorf, 1984.

[3] G. S. Eskeland Lin Gan and H. H. Kolshus. Green electricity market development: Lessons from europe and the us. *Energy Policy*, 35, 2007.

[4] M. H. Zuchrov and J. D. Hoffman. *Gas Dynamics: Multidimensional Flow*. Wiley, 1977.

[5] A. Guardone D. Pasquale, J. Harinck and S.Rebay. Geometry optimization for quasi-uniform flows from supersonic nozzles. In *V European Conference on Computational Fluid Dynamics*, Lisbon, Portugal, June 2010.

[6] A. Warren Adam. *Encyclopedia of energy technology and the environment*. Wiley, 1995.

[7] G. Angelino and P. Colonna. Multicomponent working fluids for organic rankine cycles. *Energy*, 23, 1998.

[8] G. Angelino and P. Colonna. Organic rankine cycles for energy recovery from molten carbonate fuel cells. In *35th Intersociety Energy Conversion Engineering Conference (IECEC)*, Las Vegas, NV, 2000.

[9] C. Osnaghi A. Spinelli V. Dossena, P. Gaetani and D. Colombo. Design of a test rig for organic vapors. In *Proceedings of ASME Turbo Expo 2010*, Glasgow, Scotlandl, June 2010.

[10] P. Colonna and P. Silva. Dense gas thermodynamic properties of single and multicomponent fluids for fluid dynamics simulation. *J. Fluid Eng. - T. ASME*, 125, 2003.

[11] P. A. Thompson. A fundamental derivative in gasdynamics. *Physics of fluids*, 14, 1971.

[12] P. Colonna and A. Guardone. Molecular interpretation of nonclassical gas dynamics of dense vapors under the van der waals model. *Physics of Fluids*, 18, 2006.

[13] A. Guardone and B. M. Argrow. Nonclassical gasdynamic region of selected fluorocarbons. *Physics of Fluids*, 17, 2005.

[14] P. Colonna and S. Rebay. Numerical simulation of dense gas flows in unstructured grids with an imolicit high resolution upwind euler solver. *Int .J. Numer. Meth. Fluids*, 46, 2004.

[15] V. Selmin. The node-centered finite volume approach: bridge between finite differences and finite elements. *Computer Methods in Applied Mechanics and Engineering*, 102, 1993.

[16] V. Selmin and L. Formaggia. Unified construction of finite element and finite volume discretizations for compressible flows. *International Journal for Numerical Methods in Engineering*, 39, 1996.

[17] M. Vinokur and J. L. Montangé. Generalized flux-vector splitting and roe average for an equilibrium real gas. *Journal of Computational Physics*, 89, 1990.

[18] P. Colonna and T. P. van der Stelt. Fluidprop: A program for the estimation of thermophysical properties of fluids. *software*, 2004.

[19] D. Pasquale S. Rebay, P. Colonna and A. Ghidoni. Simulation of the turbulent dense gas flow through the nozzle of an organic rankine cycle turbine. In *Proceedings of the* 8^{th} *European Turbomachinery Conference*, March 2009.

[20] E. Macchi and A. Perdichizzi. Efficiency prediction for axial-flow turbines operating with non conventional fluids. *Transaction of the ASME, Journal of Engineering for Power*, 103, 1981.

[21] R. A. Van den Braembussche J. Harinck Z. Alsalihi, J. P. Van Buijtenen. Optimization of a 3d radial turbine by means of an improved genetic algorithm. In *Proceedings of the 5th European Conference on Turbomachinery*, March 2005.

[22] T. Verstraete. *Heat transfer and multidisciplinary optimization applied on micro gasturbines*. PhD thesis, Von Karman Institute, Gent, 2008.

[23] J. Kleijnen. Kriging metamodeling in simulation: A review. *European Journal of Operational Research*, 192, 2009.

[24] A. Guardone A. Spinelli, V. Vandecauter and V. Dossena. Nozzle design for an organic vapor wind tunnel. 2010.

[25] R. A. Van den Braembussche. *Optimization and Computational Fluid Dynamics*, chapter 6. Springer, 2008.

[26] A. Guardone D. Dussin, M. Fossati and L.Vigevano. Hybrid grid generation for two-dimensional high-reynolds flows. *Computer & Fluids*, 38, 2009.